Contents lists available at ScienceDirect

Applied Catalysis B: Environmental

Photoactivity of decahedral TiO$_2$ loaded with bimetallic nanoparticles: Degradation pathway of phenol-1-^{13}C and hydroxyl radical formation

Magdalena Diak[a], Marek Klein[b], Tomasz Klimczuk[c], W. Lisowski[d], Hynd Remita[e], Adriana Zaleska-Medynska[a], Ewelina Grabowska[a,*]

[a] Department of Environmental Technology, Faculty of Chemistry, University of Gdansk, Wita Stwosza Str. 63, 80-308 Gdansk, Poland
[b] Renewable Energy Department, The Szewalski Institute of Fluid-Flow Machinery, Polish Academy of Sciences, Fiszera Str. 14, 80-231, Gdansk, Poland
[c] Department of Solid State Physics, Faculty of Applied Physics and Mathematics, Gdansk University of Technology, G. Narutowicza Str. 11/12, 80-233 Gdansk, Poland
[d] Institute of Physical Chemistry, Polish Academy of Sciences, Kasprzaka 44-52, 01-224 Warsaw, Poland
[e] Laboratoire de Chimie Physique, CNRS-UMR 8000, Université Paris-Sud, Université Paris-Saclay, 91405 Orsay, France

ARTICLE INFO

ABSTRACT

Decahedral TiO$_2$ decorated with bimetallic nanoparticles were synthesized via radiolysis and photodeposition method. The effect of bimetallic surface composition (Ag_Pt, Ag_Au, Au_Pd, Au_Pt) as well as deposition technique (simultaneous or sequential) on the photocatalytic activity in phenol degradation and efficiency of hydroxyl radicals generation under UV–vis light irradiation were investigated. Modified and pristine decahedral TiO$_2$ anatase with exposed {001} were characterized by X-ray diffraction (XRD), diffuse reflectance spectroscopy (DRS), transmission electron microscopy (TEM) with energy-dispersive X-ray (EDX) spectroscopy, scanning electron microscopy (SEM), inductively coupled plasma-mass spectrometry (ICP-MS) and X-ray photoelectron spectroscopy (XPS). The gas chromatography-mass spectrometry was employed to detect organic intermediates to establish degradation pathway of isotopically labeled (1-^{13}C) phenol. The modification with Pt and Ag nanoparticles induced an increase in photocatalytic activity of phenol degradation under UV–vis light irradiation (79% of phenol was degraded after 90 min of irradiation). The main by-products detected in phenol oxidation were catechol, hydroquinone, malonic, fumaric and maleic acid. The results indicated the formation of isotopically labeled and unlabeled maleic acid. It was noticed that all samples sequentially photodeposited on TiO$_2$ surface exhibited higher $^{\bullet}$OH radicals generation compared to pristine TiO$_2$. Our results suggest that synergistic effects between specifically engineered TiO$_2$ nanocrystals and unique properties of loaded bimetallic nanoparticles can enhance the charge separation of photoinduced carriers.

© 2016 Elsevier B.V. All rights reserved.

1. Introduction

In the past four decades titanium dioxide has been the most intensively investigated metal oxides for removing pollutants from gas and liquid streams. Among the three natural crystalline forms of TiO$_2$ (anatase, brookite and rutile), anatase TiO$_2$ has exhibited excellent properties in photocatalysis and solar energy conversion due to its more negative conduction band edge potential versus rutile TiO$_2$ [1–3]. Moreover, anatase TiO$_2$ nanocrystals with controlled sizes and shapes have been studied because of a spectrum of size-, shape-, and structure-dependent properties [4–13]. However, the performance of anatase TiO$_2$ nanocrystals depends on not only their microstructure, size and composition, but also type and the content of crystal facets [14–17]. It was proofed that it is possible to enhance activity of a specific photocatalytic reaction by controlling the kind and surface area of the exposed crystal face on semiconductor particles [18]. Recently, theoretical and experimental studies have demonstrated that, the {001} facets of anatase TiO$_2$ are much more reactive than the thermodynamically more stable {101} surface due to higher average surface energy of the {001} facets (0.90 J/m^2) than that of the {101} facets (0.44 J/m^2) [19–21]. The key to controlling the percentage of crystallographic facets of anatase crystals is to change the relative stability of each facet during crystal growth, which is intrinsically determined by the surface energies of the facets. Surface adsorbed fluorine atoms are known to be very effective in changing the sur-

face energy of TiO$_2$ facets and thus the percentage of facets [16]. Decahedral TiO$_2$ could be obtained by three main approaches: (1) hydrothermal/solvothermal route, (2) hydrolysis of TiO$_2$ precursors in ethylene glycol or (3) by gas phase reaction [22]. Among them the hydrothermal and solvothermal methods are most widely used to tailor the exposure of crystal facets due to the versatile ability in manipulating the nucleation and growth behaviors (particularly growth rates along different orientations) of crystals.

A pioneering breakthrough in the preparation of anatase TiO$_2$ with exposed {001} facets was achieved by Yang et al., who synthesized single crystallites with high percentage of {001} facets (initially 47%) from the hydrothermal reaction of the mixture of TiF$_4$ and HF [15]. With the help of 2-propanol, the percentage of {001} facets was improved to 64%, and the achieved anatase crystals were reported to generate more active hydroxyl radicals (•OH) upon UV irradiation when compared to the commercial Degussa P25 [23]. Zhang et al. obtained anatase TiO$_2$ single-crystals and observed that the photocatalytic activity increases proportionally as the level of reactive {001} facets were continuously tuned from 27 to 50% [24]. TiO$_2$ single-crystals exhibited a truncated tetragonal bipyramidal shape and the level of reactive {001} facets can be continuously tuned from 27 to 50% by changing the concentration of the ionic liquid. Furthermore, Han et al. have also confirmed that TiO$_2$ nanosheets with a higher percentage of {001} facets exhibit a more effective photocatalytic performance [11]. At the same time, Pan et al. investigated a series of anatase TiO$_2$ crystals with predominant {001}, {101}, or {010} facets, contrary to conventional understanding, they found that clean {001} exhibits lower reactivity than {101} in photo-oxidation reactions for •OH radical generation [16]. Clearly, it is still highly desirable to investigate the intrinsic correlation between photocatalytic activities and structural properties.

Lowering cost and the utilization of renewable energy requires the use of photocatalysts excited by solar radiation. One of the approach to improve TiO$_2$ photoactivity is deposition of mono- or bimetallic nanoparticles at semiconductor surface to enhance the efficiency of electron-transfer dynamic and efficiency of photocatalytic redox processes under visible light irradiation [25]. Nowadays, bimetallic nanoparticles are widely investigated because of its interesting size-dependent electrical, chemical, and optical properties. Additionally, they are important in the field of photocatalysis since they often exhibit better photocatalytic properties than their monometallic counterparts [26–32]. Although, the effect of monometallic nanoparticles (made of one noble metal) on the photocatalytic activity of TiO$_2$ is proved, however, in the case of bimetallic nanoparticles the influence of their structure and the mechanism of photocatalytic reaction still needs clarification. Bimetallic particles (BNPs) of the same size, shape, and composition show significant differences in photocatalytic activity when configured into different architectures, such as alloy or core–shell. The structure of BNPs depends on the preparation conditions, miscibility, and kinetics of the reduction of metal ions [33]. Based on the literature data it can be concluded that the most important types of bimetallic nanoparticles (Ag–Au, Au–Pd, Pt–Pd, Au–Pt, Au–Cu) play roles as follows: (1) electron trapping, (2) facilitating of electron–hole separation process, (3) promotion the interfacial electron transfer process and (4) interaction with light through an excitation of SPR to excite semiconductor [25]. Recently it was shown that TiO$_2$ loaded with Ag/Au nanoparticles or Pt/Pd revealed a higher photoactivity in phenol degradation under visible light than TiO$_2$ modified with monometallic nanoparticles [34,35]. While Kowalska et al. investigated that the Au(core)/Ag(shell)–TiO$_2$ showed reduced photoactivity compared to TiO$_2$ with individual metal deposits [36]. Au-Pd alloy, supported on TiO$_2$, was synthesized by Su et al. and used for phenol oxidation under UV light [37]. They explained that the metal nanoparticles can mediate

undesired redox reactions that ineffectively consume photogenerated radicals, thus improving the photooxidation efficiency of phenol [37]. However, it could be expected that photocatalytic activity is affected not only by the size and structure of bimetallic nanoparticles- controlled by deposition procedure—but also by the TiO$_2$ matrix, including the content of {001} facets.

In view of this, the effect of type of bimetallic nanoparticles, type of deposition method (γ radiation *versus* UV photodeposition as well as subsequent (seq) or simultaneous (both) metal precursors introducing into reaction medium) on the photoactivity of decahedral TiO$_2$ loaded with BNPs has been investigated. In this work for the first time we reported the mechanism of phenol degradation in the presence of decahedral TiO$_2$ loaded with Ag/Pt nanoparticles under UV–vis irradiation and with application of labeled carbon C^{13} isotope (phenol-1-^{13}C). To provide insight into the oxidative species participating in the degradation mechanism, hydroxyl radical test with coumarin was also studied. Based on obtained results, a possible phenol degradation pathway under UV–vis irradiation in the presence of BNPs-TiO$_2$ was proposed.

2. Experimental

2.1. Chemicals and materials

All chemicals were analytical grade and used without further purification. Titanium (IV) butoxide (TBT) (97%, Sigma-Aldrich) was used as titanium source for the preparation of decahedral TiO$_2$. KAuCl$_4$ (98%), Pd(C$_5$H$_7$O$_2$)$_2$ (99%), H$_2$PtCl$_6$·xH$_2$O(99.9%) and AgOCl$_4$(97%) from Sigma-Aldrich were used as metal source in the preparation procedure. Coumarin were purchased from Sigma–Aldrich Co. (Germany) and phenol were obtained from POCh S.A. (Poland). Ethyl chloroformate (>98% GC), pyridine anhydrous (99.8%), hydroquinone (>99.5%), malonic acid (99%), *p*-benzoquinone (>98%), fumaric acid (>99%), maleic acid (>99%) were purchased from Sigma–Aldrich Co. (Germany) where assalicylic acid and Na$_2$SO$_4$ anhydrous from Chempur Co. and Stanlab Co. respectively. Isotopically labeled (1-^{13}C) phenol was obtained from Cambridge Isotope Laboratories.

2.2. Preparation of pristine and metal-modified decahedral TiO$_2$

Decahedral TiO$_2$ nanocrystals bound by eight {101} facets and two {001} facets have been synthesized by modified solvothermal method described by Liu et al. [5]. 30 ml of hydrogen peroxide solution (30% by weight) and 4.27 ml of hydrofluoric acid (40% by weight) were added to 25 ml of tetrabutyltitanate (TBT) and stirred until creation an orange gel. Based on the literature experimental data and theoretical calculations it is well known that HF is an efficient morphology controlling agent in the field of anatase TiO$_2$ synthesis, because F ions can absorb on the particle surface to reduce the surface energy [15,38–41]. The mixture was then transferred to a 200 ml Teflon-lined autoclave and kept at 200 °C for 24 h. After solvothermal reaction, the obtained product was rinsed with ethanol and distilled water several times and then dried at 60 °C. TiO$_2$ used further for photodeposition was additionally calcined at 400 °C for 4 h.

All the modified TiO$_2$ photocatalysts were prepared by radiolytic reduction of metal ions on the surface of decahedral TiO$_2$ and by photodeposition method. Two various techniques for metal deposition were applied. First one consisted on simultaneously (both) addition of two metal precursors. For this purpose to ethanoic suspension of TiO$_2$ the two kinds of metal were introduced. Another one, relied on sequential (seq) deposition of two metals. In this case after first deposition, the second metal precursor was immediately

injected to suspension of M-TiO$_2$, which was then irradiated with γ-rays, centrifuged and dried (as shown in Table 1).

Before the radiolytic reduction process, the suspension of the photocatalyst containing metal precursor (0.5 % m/m of each: Ag, Au, Pt, and Pd, respectively) in ethanol was first stirred for about 10 min, degassed with nitrogen for 20 min, sonicated for 1 min, and finally irradiated with γ-rays (^{60}Co panoramic γ-source of 7000 curies, dose rate 4 kGy h^{-1}). Total irradiation dose depended on i.a. bimetallic composition and metal ions concentration. Collected decahedral TiO$_2$ samples modified with bimetallic nanoparticles were separated and dried at 60 °C.

In case of photodeposition method 70 ml of ethanol solution containing decahedral TiO$_2$ (1 g) and metal precursors (0.5% m/m of each: Ag, Au, Pt, and Pd, respectively) was stirred in dark under nitrogen atmosphere for 30 min, and finally illuminated under nitrogen by 250 W Xe lamp (UV flux 30.8 mW/cm^2) used as an irradiation source for 1 h. As was described above two various techniques for metal deposition were applied: simultaneously (both) and sequential (seq) reduction. Obtained samples were rinsed with deionized water and dried at 40 °C.

2.3. Characterization of TiO$_2$

The purity of the samples was confirmed with powder X-ray diffraction PXRD, X'Pert Pro MPD Philips diffractometer, with Cu Kα radiation λ = 1.5418 Å. The measurements were performed on the 2θ range of 20–80°, with the scan speed 20°./h. The lattice parameters were estimated by LeBail method using FullProf package [42].

To characterize the light-absorption properties of modified photocatalysts, diffuse reflectance (DRS) spectra in the scan range 200–900 nm were recorded. The measurements were carried out on UV–vis spectrophotometer (Evolution 220, Thermo Scientific) equipped with an integrating sphere and BaSO$_4$ was used as the reference.

Particle size, shape, dispersion uniformity and chemical composition of obtained samples have been analyzed by the transmission electron microscope with energy-dispersive X-ray spectrometer (TEM-EDX, Tecnai F20 X-Twin, FEI and EDAX spectrometer) and scanning electron microscope (SEM, Quanta 3D FEG, FEI).

Metal content was determined by inductively coupled plasma-mass spectrometry (ICP-MS) recorded using ICP-MS 7500 CX mass spectrometer (Agilent Technologies).

X-ray photoelectron spectroscopic (XPS) measurements were performed using the a PHI 5000 VersaProbe (ULVAC-PHI) spectrometer with monochromatic Al Kα radiation (hν = 1486.6 eV). The X-ray source, operating 25 W and 15 kV, was focused on 100 μm spot size, and the analyzed area was defined as a 250 μm square. The high-resolution (HR) XPS spectra were collected with the hemispherical analyzer at the pass energy of 23.5 eV, the energy step size of 0.1 eV and the photoelectron take off angle 45° with respect to the surface plane. The Casa XPS software (version 2.3.16) was used to evaluate the XPS data. The Gaussian-Lorentzian (G-L) mixed function was used to fit the experimental data. The binding energy (BE) scale of all detected spectra was referenced by setting the BE of the aliphatic carbon peak (C—C) signal to 285.0 eV.

To study the recombination of electrons–holes in the photocatalysts the photoluminescence emission spectra (PL) were measured at room temperature on a LS-50B Luminescence Spectrophotometer equipped with Xenon discharge lamp as an excitation source and a R928 photomultiplier as a detector. Obtained samples were excited with 310 nm. The excitation radiation was falling on the sample surface at an angle of 90°. Additionally, the emission filter was applied to block UV radiation above 390 nm.

Table 1
Sample label and preparation method of bare and metal modified decahedral TiO$_2$

Sample label	Type and amount of noble metal precursor used to TiO$_2$ modification		Irradiation time [h]	Efficiency of phenol degradation after 90 min irradiation [%]	ICP-MS results noble metal content [mg/g]			
	Type of precursor	Amount of precursor [m/m%]		UV–vis	Ag	Au	Pd	Pt
Prepared by radiolytic method								
Ag_Pt.TiO$_2$_R.both	AgOCl$_4$·H$_2$O/H$_2$PtCl$_6$·H$_2$O	0.5/0.5	8	66	10.31	–	–	2.48
Ag_Au.TiO$_2$_R.both	AgOCl$_4$·H$_2$O/KAuCl$_4$	0.5/0.5	5	69	8.98	2.51	–	–
Au_Pd.TiO$_2$_R.both	KAuCl$_4$/Pd(C$_5$H$_7$O$_2$)$_2$	0.5/0.5	5	73	–	2.42	2.17	–
Au_Pt.TiO$_2$_R.both	KAuCl$_4$/H$_2$PtCl$_6$·H$_2$O	0.5/0.5	5	52	–	2.58	–	2.45
Pt_Au.TiO$_2$_R.seq	KAuCl$_4$/H$_2$PtCl$_6$·H$_2$O	0.5/0.5	2.5/2.5	55	–	2.18	–	2.30
Pd_Au.TiO$_2$_R.seq	KAuCl$_4$/Pd(C$_5$H$_7$O$_2$)$_2$	0.5/0.5	2.5/2.5	74	–	1.50	1.60	–
Pt_Ag.TiO$_2$_R.seq	AgOCl$_4$·H$_2$O/H$_2$PtCl$_6$·H$_2$O	0.5/0.5	2.5/2.5	76	9.06	–	–	1.82
decahedral TiO$_2$_1	–	–	–	49	–	–	–	–
Prepared by photodeposition method (followed by calcination)								
Ag_Pt.TiO$_2$_PD.both	AgOCl$_4$·H$_2$O/H$_2$PtCl$_6$·H$_2$O	0.5/0.5	1	63	8.18	–	–	2.72
Ag_Au.TiO$_2$_PD.both	AgOCl$_4$·H$_2$O/KAuCl$_4$	0.5/0.5	1	66	6.86	1.89	–	–
Au_Pd.TiO$_2$_PD.both	KAuCl$_4$/Pd(C$_5$H$_7$O$_2$)$_2$	0.5/0.5	1	56	–	2.73	1.35	–
Au_Pt.TiO$_2$_PD.both	KAuCl$_4$/H$_2$PtCl$_6$·H$_2$O	0.5/0.5	1	47	–	2.58	–	2.15
Pt_Au.TiO$_2$_PD.seq	KAuCl$_4$/H$_2$PtCl$_6$·H$_2$O	0.5/0.5	1/1	63	–	2.0	–	2.03
Pd_Au.TiO$_2$_PD.seq	KAuCl$_4$/Pd(C$_5$H$_7$O$_2$)$_2$	0.5/0.5	1/1	62	–	2.51	1.67	–
Pt_Ag.TiO$_2$_PD.seq	AgOCl$_4$·H$_2$O/H$_2$PtCl$_6$·H$_2$O	0.5/0.5	1/1	78	7.39	–	–	3.03
decahedral TiO$_2$_2	–	–	–	66	–	–	–	–

2.4. Measurement of photocatalytic activity in the aqueous phase

The photoactivity of the obtained samples was estimated by measuring the rate of phenol decomposition in an aqueous solution in the presence of visible and UV–vis irradiation described in our previous study [43]. The detailed characterization procedures can be seen in the Supplementary material. Photocatalytic degradation runs were preceded by blind test in the absence of a photocatalysts or illumination. No degradation of phenol was observed in the absence of either the photocatalyst or illumination

2.5. Intermediate analysis of phenol-1-^{13}C

By-products formed during phenol degradation were identified by GC–MS technique. The initial concentration of phenol for intermediate product identification study was 100 ppm. Higher initial concentration of phenol increased possibilities of isolation and identification of by-products. GC–MS analysis was performed using the Shimadzu single quadrupole GC–MS-QP2010 SE gas chromatograph-mass spectrometer equipped with 30 m ZB-5MSi capillary column. A 1 μL aliquot was injected in the splitless mode with injection temperature 230 °C. The temperature program of the column was adjusted: 50 °C for 1 min, followed by ramp to 180 °C at 7 °C/min. Helium was used as carrier gas with constant flow rate 1.16 ml/min. The ion source was set to 200 °C and the interface temperature was held at 250 °C. Qualitative evaluation was conducted using scan or sim mode sometimes in order increase sensitivity higher voltage of detector was set.

The collected samples were treated with ethyl chloroformate (ECF). Derivatization was carried out as follows: 0.2 ml of the sample and medium consisted of 0.1 ml of ethanol, 0.02 ml of pyridine, 0.03 ml of 0.1 M HCl and 0.05 ml of ECF was mixed and left for 15 min. Subsequently, 0.2 ml of chloroform was added and after shaking the organic phase was removed and dried with anhydrous Na_2SO_4.

2.6. Formation of hydroxyl radicals

The formation of hydroxyl radicals in a suspension of TiO_2 under UV–vis irradiation was evaluated by a photoluminescence (PL) technique using coumarin as a probe molecule, which readily reacted with •OH radicals to produce the highly fluorescent product, 7-hydroxycoumarin. Formation of hydroxyl radicals was estimated using the same experimental set-up as for measuring decomposition rate of phenol under UV–vis light [43]. The concentration of TiO_2 and coumarin were 0.5 g/dm^3 and 10^{-4} M, respectively. After irradiation, the solution was filtered and analyzed on a LS-50B Luminescence Spectrophotometer equipped with Xenon discharge lamp as an excitation source and a R928 photomultiplier as a detector by excitation with radiation of a wavelength of 330 nm.

3. Results and discussion

3.1. Morphology

Sample labels together with preparation conditions and samples' characteristics are listed in Table 1, while the morphology of pristine decahedral TiO_2 and the most active sample (the Pt_Ag_TiO_2_PD_seq sample) is shown in Fig. 1 A–D, respectively.

Fig. 1A and B show that obtained product is composed of a large quantity of uniform TiO_2 nanocrystals with truncated bipyramid-shape. The thickness and side length of the TiO_2 nanocrystals are in the range of 70–100 nm and 40–50 nm, respectively. According to the crystallographic symmetry of anatase TiO_2, the truncated bipyramid-shaped TiO_2 nanocrystals are bound by eight {101}

facets and two parallel {001} facets (the inset in Fig. 1B). Decahedral TiO_2 obtained in this study were larger than the ones obtained by Liu et al. (thickness in the range of 20–40 nm and side length −60–80 nm) [5]. Liu et al. obtained anatase TiO_2 particles ranging from 30 to 85 nm [44].

The inset in Fig 1C shows a typical SAED image taken from an individual Pt_Ag_TiO_2_PD_seq sample. The fringe spacing, which is the interplanar separation between the growth direction planes of the nanocrystal, could be estimated as 0.235 nm, so the SAED pattern confirms that the obtained products exhibit single-crystal characteristics and indicates that the top and bottom surfaces of the single crystals are the {001} facets [11,45–48]. In order to analyze the type of metallic platinum and silver plane, selected area electron diffraction was applied. The Pt and Ag NPs TiO_2 sample showed a characteristic region {200} and {111} plane of metallic platinum (d = 0.190 nm) and silver (d = 0.237 nm), respectively.

In order to determine the exact amount of the bimetallic NPs in each sample, all photocatalysts were analyzed by using Inductively Coupled Plasma-Mass Spectrometry (ICP-MS). The content of the metal in each BNPs-TiO_2 is expressed as the mass of the metal components (in milligrams) per 1 g of a sample and listed in Table 1. Slightly disagreement between the theoretically calculated BNPs loadings and those measured by ICP-MS, can be assigned to incomplete reduction of noble metal. In case of samples modified by Ag NPs the average silver content was about 8.5 mg/g. While, the average content of Au, Pd and Pt was about 2.3; 1.7 and 2.4 mg/g, respectively.

3.2. Crystal structure and UV–vis properties

Crystalline phase composition of the bimetallic nanoparticles deposited at the TiO_2 surface was studied by the powder x-ray diffraction (PXRD) technique. The PXRD measurements were conducted on PhillipsX'Pert Pro MPD diffractometer with CuKα radiation. The results were processed by means of LeBail refinement using FULLPROF 5.30 software. All PXRD patterns look very similar, e.g. the only refined phase was TiO_2 and no traces of noble metals were observed. Fig. S1 in Supporting information presents a typical PXRD pattern with the LeBail refinement for a decahedral TiO_2 sample.

The lattice constants do not change much in the series with the lowest values a = 3.7846(1) Å, c = 9.5079 Å, and the largest a = 3.79025(6) Å, c = 9.5220(2) Å, estimated for the decahedral TiO_2 and Pt_Ag_TiO_2_PD_seq samples, respectively. The average crystallite size was calculated using the Scherrer equation. The smallest crystallites (d ∼ 110 nm) were found for Pt_Au_TiO_2_R_seq, whereas twice larger crystallites (d ∼ 220 nm) were observed for the Pt_Ag_TiO_2_R_seq and Au_PdTiO_2_Pd_both samples.

The diffusion reflection spectra of bimetallic nanoparticles modified TiO_2 photocatalysts are shown in Fig. S2 in the Supporting information. The spectra of the all obtained bimetallic nanoparticles immobilized on TiO_2 except Ag_Au_TiO_2_R_both show an increase in the absorbance at wavelengths longer than 400 nm. By immobilizing the bimetallic nanoparticles, the energy level of the valence bands of the photocatalysts is shifted to lower energy. This results in more absorption at longer wavelengths and causes an improvement in the photocatalytic activities under Vis illumination. However, a link between these spectral features and the observed photocatalytic performances has not been proved.

Noble metal nanoparticles, such as gold, silver, platinum and palladium possess the ability to absorb visible light due to localized surface plasmon resonance (LSPR). The surface plasmon resonance in silver and gold nanoparticles can be referred to free conduction electrons at metal surface (d electrons) and overlapped d-electrons, s-electrons, p-electrons in platinum and palladium, which exhibit intrinsic Fano interference [49]. The Ag-TiO_2 and Au-TiO_2 nanopar-
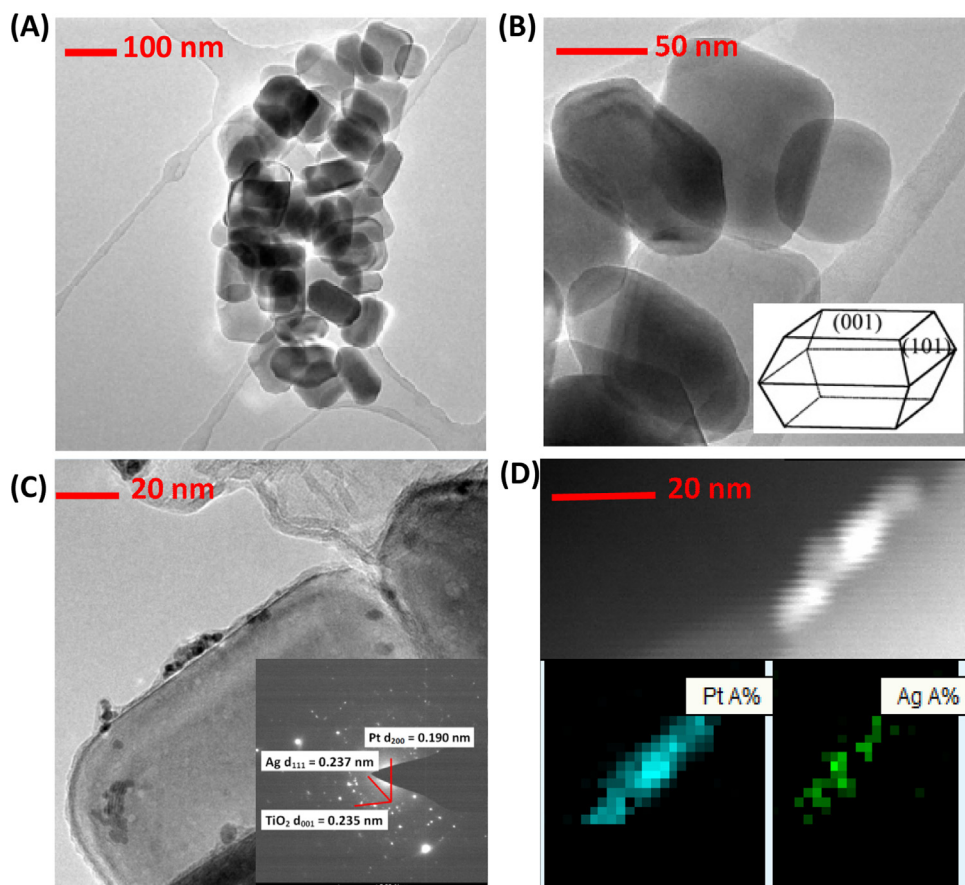
Fig. 1. TEM analysis of pure decahedral TiO_2 nanoparticles (A and B), and TEM analysis of Pt_Ag_TiO$_2$_PD_seq sample: (C) TEM and SAED image, (D) TEM and mapping analysis.

ticles show plasmon absorption bands at about 410 and 560 nm, respectively [29,31,50]. For Pd and Pt nanoparticles deposited on TiO_2 surface Zielińska et al. observed localized surface plasmon resonances over a wide spectral range from near-UV through the visible region and even into mid-IR due to overlapping interband continuum with the plasmon resonance for Pt nanoparticles [35]. For obtained decahedral TiO_2 modified with BNPs no surface plasmon was observed for any of prepared samples. Based on the literature data it knows that the absorption band of the bimetallic nanoparticles could not be obtained by simple overlapping of the absorption bands of monometallic nanoparticles deposited on the TiO_2 surface. Cybula et al. synthesized TiO_2 modified with Au/Pd nanoparticles and reported that characteristic SPR absorption of gold was evident in the case of Au/Pd bimetallic nanoparticles, since these particles contain gold in excess (Au:Pd = 12.5:1), while for samples with higher palladium to gold ration (Au:Pd = 2.5:1) plasmonic band is suppressed [31].

3.3. XPS analysis

The XPS characterization of the Pt_Ag_TiO$_2$_PD_seq sample has been performed. This sample proved to be the most active among photocatalysts synthesized by sequent addition of two metals. Table 2 shows the composition and chemical characters of elements formed in the surface layer of this sample. It is important to note that the elemental composition evaluated by XPS is evaluated only within a surface region, in a depth limited by the elemental detection range of XPS analysis. This relationship is well described by the inelastic mean free paths (IMFP) of photoelectrons [51]. For photoelectrons emitted from Ag 3d$_{5/2}$ and Pt 4f$_{7/2}$ signals the IMFP value can be estimated to be 1.54 nm and 1.68 nm, respectively [51].

Titanium, oxygen, carbon, platinum, silver and chlorine were detected and corresponding high-resolution (HR) XPS spectra of Ti 2p, O 1s, C 1s, Pt 4f, Ag 3d and Cl 2p are presented in Fig. 2. Two chemical states of titanium were separated in the Ti 2p spectrum at the BE of Ti 2p$_{3/2}$ peak 459.1 eV and 457.6 eV, which can be identified as Ti^{4+} and Ti^{3+}, respectively [52,53]. The O 1s spectrum can be composed of three different peaks, at BE of 530.3 eV, 531.3 eV and 532.5 eV, which can be described as bulk (TiO$_{latt}$), surface (TiO$_{surf}$) states of TiO_2 and —OH groups, respectively [54,55]. First peak can be also accompanied by coexistence of Ag$_x$O species and second one by PtO$_x$ and C=O compounds [55]. The C 1s region can be deconvoluted for three peaks, at BE of 285.0 eV, 286.6 eV and 289.1 eV, which can be attributed to C—C, C—O and C=O bounds, respectively [55,56].

The XPS spectrum of Ag 3d, detected in the Pt_Ag_TiO$_2$_PD_seq sample, indicate only one Ag 3d$_{5/2}$ component at BE 367.5 eV. The peak position shows a negative energy shift as compared to pure Ag (367.9–368.4 eV), what is characteristic for Ag$^+$ species formation [55,57].

The deconvolution of Pt 4f spectra is complicated by overlapping with Ti 3s satellite peak. Thus, the fit parameters of the last peak have been revealed from separate Ti 3s spectrum recorded on pristine TiO_2 sample. As a result, four Pt states, represented by Pt 4f$_{7/2}$ signals at BE 70.7 eV, 71.6 eV, 72.5 eV and 73.7 eV, can be identified. First one corresponds to Pt at zero valent state [55,58,59]. Moreover, because the BE values originated from pure Pt (70.6–71.3 eV) are very close to AgPt alloys (70.2–71.3 eV), we should also consider formation of AgPt bimetal components at this Pt state [55,60]. The BE position of second peak can be considered as a result of the BNPs interaction with TiO_2 matrix environment leading to surface PtTix species formation [55,61]. Third Pt 4f$_{7/2}$ signal can be originated
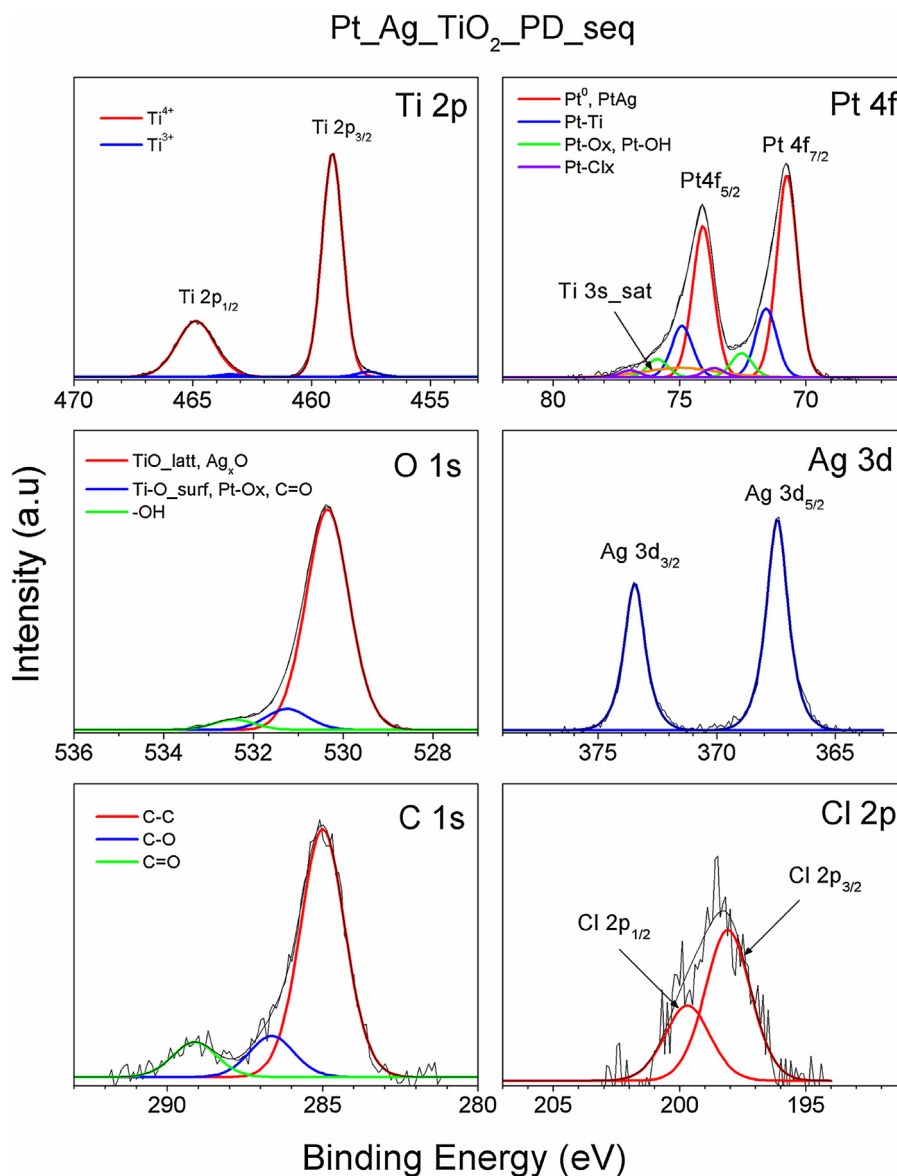
Fig. 2. XPS spectra of Ti 2p, O 1s, C 1s, Ag 3d, Pt 4f and Cl 2p for Pt_Ag_TiO$_2$_PD_seq sample.

from Pt-OH bound and oxidized Pt surface compounds [55]. The last deconvoluted Pt 4f$_{7/2}$ peak can be assigned to chorine interaction with Pt component of bimetal AgPt nanoparticles [55].

The Pt atoms at surface region seems to be partially bound to chlorine adatoms forming Pt-Cl$_x$ compounds. The presence of chlorine surface species is also evidenced by Cl 2p spectra shown in Fig. 2. Their formation affects the Ag/Pt atomic ratio at surface region. As shown in Table 2, the platinum content in the Pt_Ag_TiO$_2$_PD_seq sample was found to be larger than Ag surface contribution. However, taking the atomic content of chlorine from Table 2 (1.1 at.%) and assuming the PtCl$_2$ formation, we can roughly estimate the number of Pt atoms bound to Cl to be 0.55 at.%. Subtracting this value from the total content of Pt (1.86 at.%) we get the Pt atoms contribution value close to Ag surface content (1.31 at.%, Table 2). This result fits well the AgPt bimetal formation at the surface layer of the Pt_Ag_TiO$_2$_PD_seq sample.

3.4. Photocatalytic activity in phenol decomposition

Phenol was chosen as a model pollutant due to its high toxicity and very difficult degradation process. Furthermore, the carcino-genicity of phenol derivatives demands their prompt removal from the water in order to avoid the contact with living organisms [62]. The phenol could be first photodegraded into some intermediates, such as hydroquinone, pyrocatechol, 1,2,4-benzenetriol, pyrogal-lol, and 2-hydroxy-1,4-benzoquinone, which are finally converted into CO$_2$ and H$_2$O. However, toxicities of hydroquinone (HQ) and benzoquinone (p-BQ) are much higher than that of phenol itself, therefore it is necessary to clarify the degradation and mineral-ization pathway of phenol [63]. In our previous study, efficiency of phenol degradation as well as formation of phenol degradation by-products were evaluated in the presence of tungsten-modified TiO$_2$ nanoparticles [64]. Obtained results showed a different degra-dation mechanism of phenol in the presence of W-doped TiO$_2$ and visible light than in UV and pristine TiO$_2$ system. For P-25/UV sys-tem, catechol was detected as the main hydroxylation by-product. Moreover, muconic acid, muconic aldehyde and maleic acid were identified as the phenol ring cleavage products. Phenol irradiation by visible light in the presence of suspended W-TiO$_2$ still leads to formation of hydroxyproducts (catechol) and phenol ring cleavage products (muconic aldehyde) [64].

Table 2
Chemical character and amount of Ag, Au, Pt and Ti atoms incorporated into surface layer of Pt_Ag_TiO2_PD_seq, decahedral TiO2_1 and decahedral TiO2_2 sample.

Sample label	Ag content (at.%)	Fraction Ag 3d$_{5/2}$ state (%)		Pt content (at.%)	raction Pt 4f$_{7/2}$ state (%)				Ti content (at.%)	Fraction Ti 2p$_{3/2}$ state (%)		O content (at.%)	C content (at.%)	Cl content (at.%)
		Ag^0 (368.5 eV)	Ag^{1+} (367.5 eV)		Pt^0, Pt (70.7 eV)	Pt-Ti (71.6 eV)	Pt-Ox, Pt-OH (72.5 eV)	Pt-Clx (73.7 eV)		Ti^{4+} 459.0 eV	Ti^{3+} 457.4 eV			
Pt_Ag_TiO2_PD_seq	1.32	0	100	1.86	66.35	22.58	7.98	3.09	26.02	97.36	2.64	59.23	10.47	1.1
decahedral TiO2_1	–	–	–	–	–	–	–	–	27.03	98.40	1.60	60.61	12.36	–
decahedral TiO2_2	–	–	–	–	–	–	–	–	28.57	96.04	3.96	63.54	7.89	–

In the present studies, the efficiency of UV–vis-induced degradation of phenol was measured over BNPs-anchored decahedral TiO$_2$ prepared by: (1) radiolytic and (2) photodeposition methods. Before the photodeposition, pristine TiO$_2$ were pre-treated by calcination.

It is known that the promoting effect of bimetallic nanoparticles is attributed to either the improved spatial charge separation in TiO$_2$ semiconductor or charge carrier transfer from metal NPs to conduction band of TiO$_2$ as well as it is related to the electronic and geometric effects [25,26]. Moreover, for TiO$_2$ photocatalysts modified with bimetallic NPs the mechanism of photocatalyst excitation depends on bimetallic nanoparticles structure, and in photocatalysis rather alloyed NPs seem to be beneficial than that of core–shell [25,26,31].

For samples obtained by radiolytic reduction, it was observed that the decoration of TiO$_2$ with bimetallic nanoparticles has contributed to the increased photocatalytic activity. For the photocatalysts, in which metal precursors were introduced simultaneously, the highest photoactivity showed the Au_Pd_TiO$_2$_R_both sample (after 90 min of irradiation the degradation efficiency of phenol increased up to 73%,see Table 1). In the case of second group of photocatalysts, which were obtained in two-step sequential deposition, the highest UV–vis activity was observed for the Pt_Ag_TiO$_2$_R_seq sample (76 % of phenol was degraded). Nonetheless, photocatalyst modified with palladium and gold exhibited almost the same phenol decomposition efficiency (74% of phenol was removed after 90 min of irradiation). Referring results of photoactivity of BNPs modified TiO$_2$ to the activity obtained for pristine TiO$_2$, all samples showed superior properties compared to unmodified TiO$_2$. In the presence of pristine decahedral TiO$_2$ 49% of phenol was degraded. Klein et al. modified P25-TiO$_2$ with bimetallic clusters (Ag/Pt, Ag/Pd and Pd/Pt) by simultaneous or subsequent γ-rays reduction and suggested that the direct electron transfer from bimetallic nanoparticle to the conduction band of TiO$_2$ takes place under visible light irradiation [65]. Photocatalytic activity of synthesized samples was investigated by photocatalytic degradation phenol under Vis (λ > 420 nm) light illumination. In the case of sequential metal deposition the highest activity during phenol degradation process was achieved by the Pt/Pd-TiO$_2$ sample containing 0.1 wt.% of each metal (ca. 15% after 60 min). Among the photocatalysts obtained in simultaneous metal deposition method, the Pt/Pd-TiO$_2$ sample exhibited the highest photocatalytic activity (ca. 16% after 60 min) [65].

In present research the second group of photocatalysts was synthesized by photodeposition method and the same concentration and combination of noble metals were applied as for radiolytic reduction. Among the photocatalysts obtained in single step, the highest activity showed TiO$_2$ modified with silver and gold. In the presence of Ag_Au_TiO$_2$_PD_both sample, 66% of phenol was degraded after 90 min of irradiation. In the case of samples synthesized by sequential reduction of two metals, the most promising activity revealed photocatalyst with platinum and silver. In the presence of Pt_Ag_TiO$_2$_PD_seq photocatalyst the degradation efficiency reached 78% after 90 min of UV–vis irradiation. Generally, most of calcined decahedral TiO$_2$ samples decorated with BNPs showed the deterioration of photocatalytic activity in comparison to unmodified TiO$_2$. The photoactivity decreased up to 63, 56, 47, 63, 62% for samples the Ag_Pt_TiO$_2$_PD_both, Au_Pd_TiO$_2$_PD_both, Au_Pt_TiO$_2$_PD_both, Pt_Au_TiO$_2$_PD_seq and Pd_Au_TiO$_2$_PD_seq, respectively. Enhanced activity of unmodified titania could be attributed to the presence of O-vacancies created during calcination process. These oxygen vacancies play an important role in oxidation reactions since oxidative species, such as superoxide and peroxide ones, are formed from them by reaction with molecular oxygen [66,67]. Calcination at 400 °C for 4 h could induce formation of highly crystalline anatase phase. To confirm

that the increase in activity is due to the presence of oxygen vacancies, the XPS analysis of decahedral TiO_2 before and after calcination was performer (see Table 2). Oxygen vacancies (O_v) can be understood as unpaired electrons, which were located initially in an O 2p orbital [68]. Literature data have shown that water molecules predominantly dissociate at the O_v sites, resulting in the formation of paired hydroxyl groups. Additionally, charge transfer from the 3d Ti orbitals of Ti^{3+} to the molecular π-orbitals of OH is observed [68]. Because for sample calcined at 400 °C for 2 h the amount of Ti^{3+} fraction is almost 2.5 times higher than for non-calcined samples, we can assumed that Ti^{3+} and oxygen vacancies may be responsible for the enhanced visible-light absorption.

It was stated that modification with BNPs promotes charge carriers separation under UV irradiation, by transfer of photogenerated electrons from the conduction band of TiO_2 to noble metal nanoparticles. It was noticed that modified photocatalysts prepared by sequential deposition showed superior photocatalytic activity in comparison to pristine TiO_2 [69]. Kowalska et al. examined the influence of photodeposition techniques on photocatalytic properties of TiO_2 based photocatalysts [36]. Simultaneous and successive deposition of silver and gold on the surface of three commercial available titania photocatalysts (rutile (TIO-6, Ald_R) and anatase (ST-41)) have been investigated [36]. Evaluation of the photocatalytic activity was conducted during methanol dehydrogenation and 2-propanol oxidation under UV and visible light irradiation (λ > 450 nm), respectively. The results showed that modification of small rutile (TIO-6) and large anatase (ST-41) titania's surface with two noble metals may cause a decay in photocatalytic activity of TiO_2. Titanium dioxide decorated by monometallic nanoparticles demonstrated much higher photoactivity than that one loaded by bimetallic nanoparticles. Additionally, it was noticed that photoactivity increased in the presence of large rutile titania (Ald_R) when second metal was successively deposited on the surface of monometallic-modified titania. Modification of titania in the form of smaller nanoparticles (TIO-6, ST-41) resulted in a decrease in photoactivity independently on deposition technique. Photocatalysts obtained by successive and simultaneous deposition of noble metals on TiO_2 with large primary particle size, showed the increased and reduced photoactivity, respectively. They clarified that electronic rather than energy transfer mechanism is responsible for plasmonic photocatalytic activity under visible light irradiation [36]. Tada et al. also concluded that photocatalytic activity is attributed to surface electronic properties of the noble metals [70]. In contrast to Kowalska's research Yu et al. synthesized gold and palladium modified surface of TiO_2 nanotube film by simultaneous photodeposition [71]. In order to estimate the photocatalytic activity of Au/Pd-TiO_2 organophosphorus pesticide malathion has been chosen as a model compound and degraded under UV light irradiation. It has been noticed that modified photocatalysts revealed higher degradation efficiency than unmodified TiO_2. 98 % and near 74% of malathion was removed in the presence of Au/Pd-TiO_2 and pristine TiO_2, respectively [71]. Sclafani et al. photodeposited 0.5 wt.% of silver and palladium on both anatase and rutile surface [72]. In these study, photocatalytic oxidation of isopropanol in TiO_2 suspension under the irradiation UV–vis light was investigated. Noble metal modified anatase exhibited 3 times higher activity than that of modified rutile-TiO_2. They suggested that the reaction relied on common electronic process whereby photogenerated electrons in conduction band of titania can transfer to silver and platinum [72].

Summarizing, the highest photoactivity under UV–vis light irradiation was observed for the Au_Pd_TiO_2_R_both and Pt_Ag_TiO_2_R_seq samples obtained by simultaneous and successive radiolytic reduction, respectively. Photocatalysts prepared by photodeposition method, where the noble metals were introduced sequentially, revealed higher photocatalytic activity. It was

previously reported that deposition of two metals in single step may result in formation of core-shell or alloy like structure which favor charge carriers recombination [36]. Based on this finding, we can deduce that higher degradation efficiency of samples prepared in two step is caused by generation of individual metallic crystallites. It was observed that, photocatalytic activity under UV–vis irradiation could also depend on titania source.

3.5. Analysis of phenol-1-^{13}C degradation intermediates

To identify phenol degradation by-products, phenol aqueous solution was irradiated for 5 h by UV–vis light (λ > 350 nm) in the presence of suspended BNPs-TiO_2. The commercial standards were analyzed by GC–MS technique under the same conditions as the degradation compounds of isotopically labeled (1-^{13}C) phenol. Retention times and mass spectra of target samples and standards were compared. Analytes were derivatized with ethyl chloroformate (ECF) as it was described in experimental section. Compared to unlabeled reference substance, the masses of the molecular peak and the respective fragment peaks of isotopically labeled (1-^{13}C) phenol and its degradation intermediates were increased by one mass unit.

GS-MS analysis revealed that only small amounts of benzene ring cleavage products were formed after 300 min irradiation. Therefore, selected ion monitoring mode was applied for quantification of salicylic and short chain dioic acids. The measurements of phenol degradation process were performed using 1000 W Xenon lamp with the intensity of 3 mW/cm^2. Decahedral titania supported silver and platinum nanoparticles obtained by sequential photodeposition method, revealed the highest photocatalytic activity. For this reason, degradation measurement in the presence of the Pt_Ag_TiO_2_PD_seq sample was repeated with higher light intensity, equaled 24.3 mW/cm^2. Table 3 presents the main intermediates identified over selected photocatalysts suspensions after 300 min irradiation. Because of the superior activity of the Pt_Ag_TiO_2_PD_seq sample, all TiO_2 modified with Pt and Ag NPs were chosen to explain the mechanism degradation of phenol-1-^{13}C.

GC–MS analysis of the reaction mixture indicated formation of maleic acid consisted of two different carbon atoms: ^{13}C (with the base peak at $m/z = 100$) and ^{12}C (with the base peak at $m/z = 99$). The ratio between the relative intensities of characteristics ion fragments reflected the relative proportion of ^{13}C-labeled to ^{12}C-unlabeled degradation by-products. Photocatalytic degradation over noble metals modified titania leads to formation of maleic acid with the base peak at $m/z = 100$. However, a fragment ion with $m/z = 99$ (with abundance from 72 to 94%) significantly increased in the mass spectra. These results suggested that reaction mixture is consisted of maleic acids contained ^{13}C carbon isotope and unlabeled ^{12}C species. It can therefore be concluded that ^{13}C-labeled maleic acid could be generated by the decomposition of hydroquinone (see Fig. 3 pathway I), while unlabeled maleic acid by the degradation of catechol (see Fig. 3 pathway II). However experiment conducted with 8 times higher lamp power showed formation only unlabeled components in the presence of the Pt_Ag_TiO_2_PD_seq sample. Application of more powerful radiation source caused formation higher amount of unlabeled maleic acid with only some residue of labeled compound. None of other short chain dioic acids were observed, an exception was noticed for the last test, when due to higher illumination intensity the higher concentration of degradation by-product was established. Malonic and fumaric acid with existence only unlabeled carbon atom were identified over Pt_Ag_TiO_2_PD_seq photocatalyst. There is no doubts that phenol derivatives like catechol and benoquinone with a fragment base peak at $m/z = 111$ were consisted of only ^{13}C carbon

Table 3
The main identified products by GC–MS after UV–vis irradiation for 300 min in the presence of pristine decahedral TiO$_2$ and decorated by Ag/Pt BNPs.

Retention times	Identified products	Chemical structure	Sample label with base peak m/z (relative peak intensity)					
			decahedral TiO$_2$_2	Ag_Pt_TiO2_PD_both	Pt_Ag_TiO2_PD_seq	Ag_Pt_TiO2_R_both	Pt_Ag_TiO2_R_seq	Pt_Ag_TiO2_PD_seq*
6.7	propenodioic acid, diethyl ester (malonic acid)		–	–	–	–	–	115, 116 (29)[a]
7.7	2-butanedioic acid (Z) (maleic acid)		99, 100 (72)	99 (94), 100	99 (70), 100	99 (87), 100	99 (75), 100	99, 100 (17)
7.8	2-butanedioic acid (E) (fumaric acid)		–	–	–	–	–	127, 128 (14)
8.8	2-hydroxybenzoic acid (salicylic acid)		120 (55), 121	120 (47), 121	120(46), 121	120 (53), 121	120 (46), 121	120 (66), 121
13.9	1,2-benzenodiol (catechol)		110 (13), 111	110 (13), 111	110 (11), 111	110 (11), 111	110 (11), 111	110 (22), 111
15.5	1,4-benzenodiol (hydroquinone)		110 (21), 111	110 (20), 111	110 (21), 111	110 (20), 111	110 (21), 111	110 (22), 111

Pt_Ag_FD_seq* experiment repeated with higher lamp power (I = 24.3 mW/cm^2 with optical filter − 350 nm).

[a] Underlined value corresponds to the base peak; in bracketswas showna relative peak intensity of the second main molecular ion.
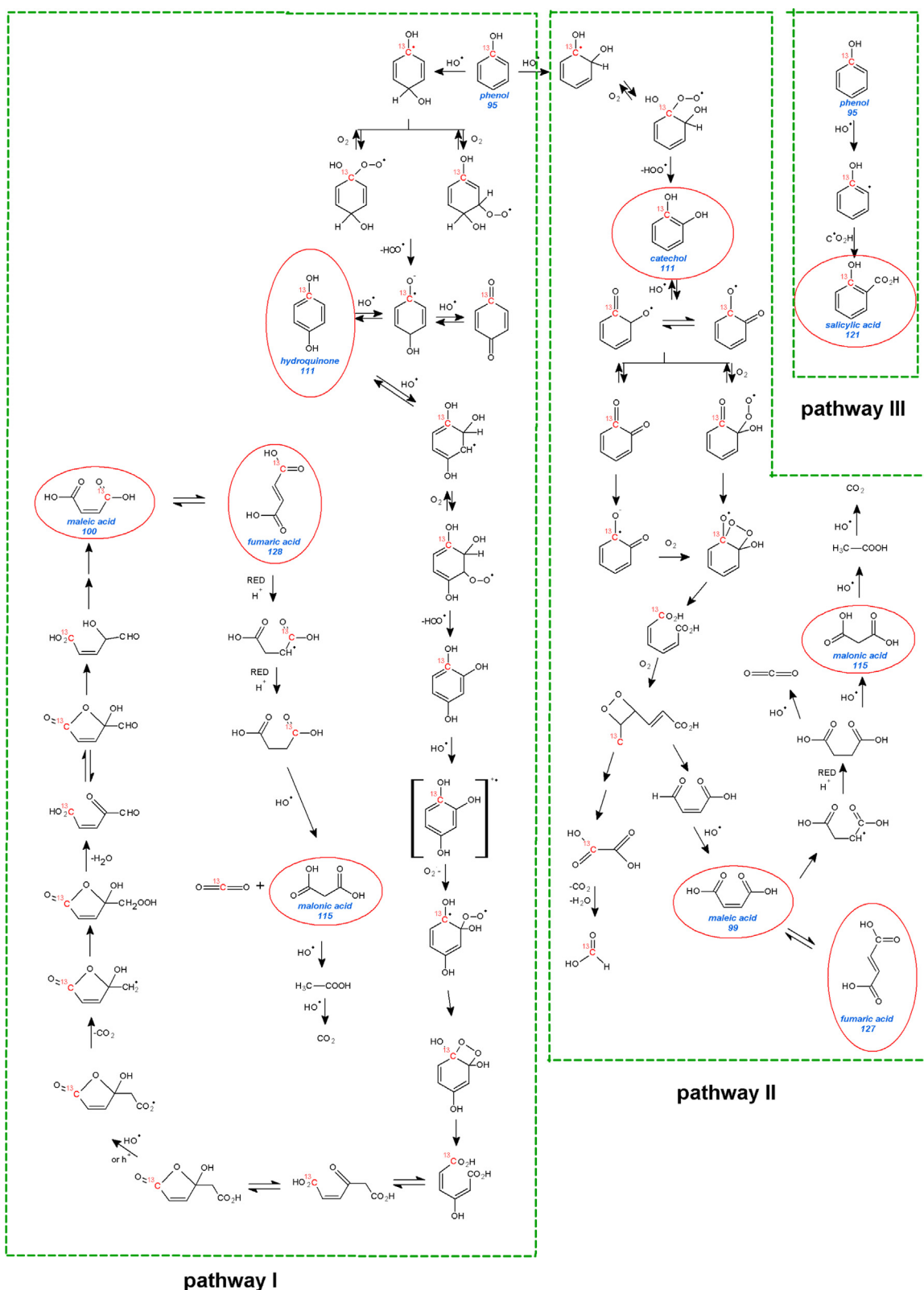
Fig. 3. Most probably pathways for photocatalytic degradation of phenol-1-^{13}C in the presence of pristine decahedral TiO$_2$ and decorated by Ag/Pt BNPs.

isotope. Based on the literature probable mechanism of phenol degradation was proposed and described.

Phenol degradation typically proceeds *via* electrophilic attack promoted by hydroxyl radicals or by direct hole oxidation of the surface-bond substrate [73]. It is supposed that most of organic radicals created in the first step react with O$_2$. However reaction with superoxide or hydroperoxyl radical is even more credible for organic compounds oxidized in the neighborhood of a TiO$_2$ particle (because of the high local level of the oxygen species) [73].
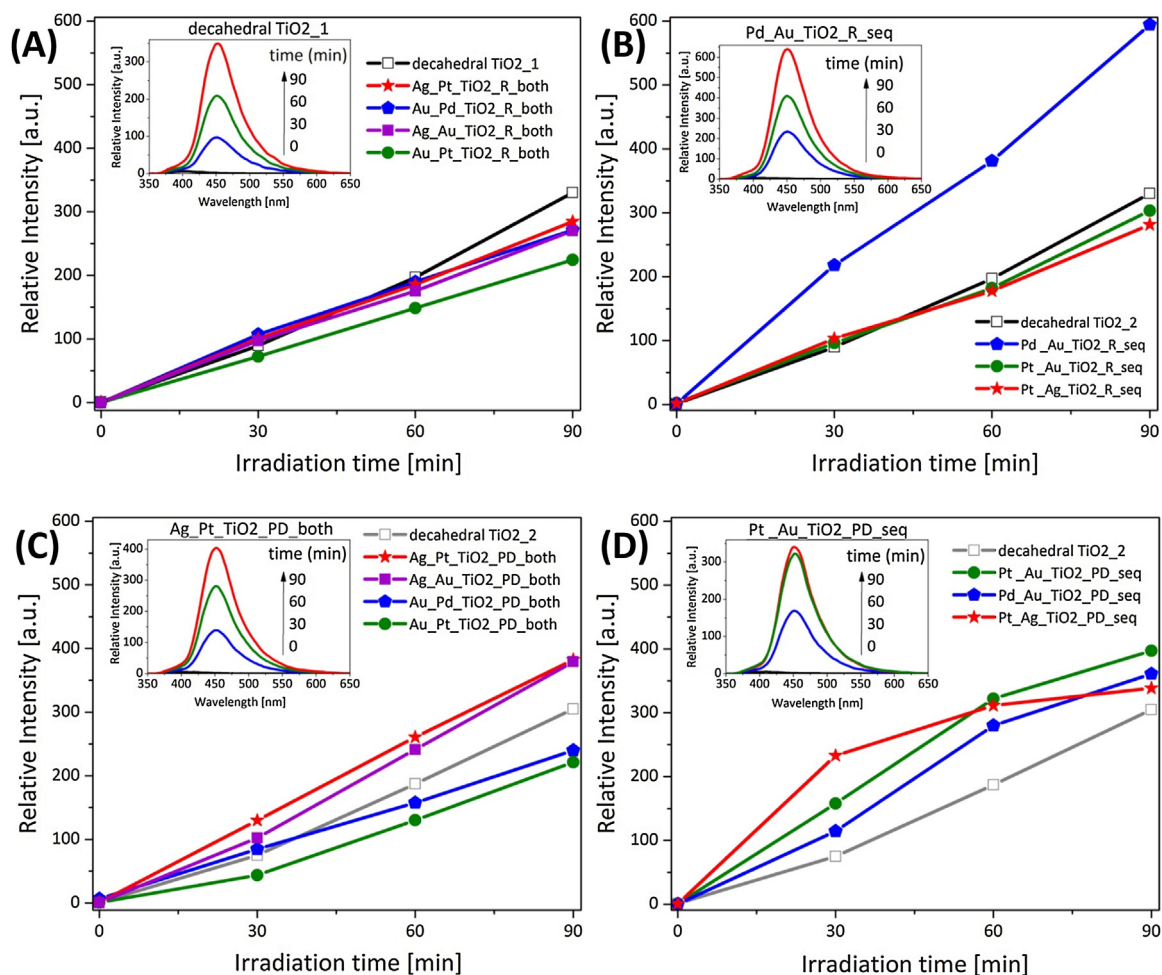
Fig. 4. Plots of the induced PL intensity at 456 nm against irradiation time for coumarin solution (10^{-3} M) on the prepared decahedral TiO_2 modified with bimetallic NPs obtained by (A) both and (B) seq radiolysis method and (C) both and (D) seq photodeposition method. Inset: PL spectral changes observed during illumination for the most active photocatalysts.

Literature data shows that •OH addition occurs preferential to the ortho and *para*-positions [74]. Formed that way dihydroxycyclohexadienyl radicals react with oxygen and release HO_2 •/O_2• [75]. These reactions result in the formation of hydroquinone and catechol as we can see in Fig. 3 (pathway I and II). Further hydroxylation of hydroquinone could induce formation of benzenetriol which presumably arises by addition of •OH, reaction with O_2 and elimination HO_2 [73]. Richard et al. and also Li et al. confirmed that benzoquinone is not the most important agent. Benzoquinone can be rapidly reduced to hydroquinone in the presence of TiO_2 under irradiation [73,76]. Li et al. suggested that 1,2,4-benzenotriol is oxidized faster than hydroquinone due to reaction with O_2, and the oxidation could be completed in short time under alkaline environment. The reaction runs slower or is even incomplete under neutral or acidic conditions [73]. Li et al. carried out the degradation of 1,2,4-benzenotriol in the suspension of TiO_2 at various pH equals 2.3, 4.5, 7.0 and 8.5. "Black light" lamps with emission centered at 360 nm were used as the irradiation source. The 1,2,4-benzenetriol was degraded after 1 h of illumination. The total organic carbon (TOC) decreased faster in the lower pH, reached 20% after 500 min at pH 8.5 and zero after 300 min at pH 2.3 [73]. Our data indicate distribution between the quantity of generated isotopically labeled and unlabeled maleic acid. These results may suggests that further photodegradation of hydroquinone may lead to formation of relatively smaller amount of ^{13}C-labeled maleic acid. Li et al. suggested that only very small portion of hydroquinone undergoes ring cleav-

age [73]. In the case of hydroquinone hydroxylation is the prevailing reaction. It is supposed that ring opening reaction is more significant for benzenetriol. Literature data shows that trioxygenated benzene presumably reacts with hydroxyl radicals or its surface-bond equivalent *via* electron transfer. The same product can be obtained by two ways: one-electron oxidation caused by addition of •OH followed by elimination of water or single electron transfer. It is proposed that as created organic radical cation reacts with superoxide, which acts as the trapping agent [73]. This way formed intermediates have zwitterionic character. Generated dioxoetanes decomposed to the acid-aldehyde or the diacid. Li et al. claimed that diacid is the main byproduct and only some traces of acid-aldehyde cleavage product is formed. This dienoicacid is oxidized *via* direct reaction with h+ or •OH followed by decarboxylation by the photo Kolbe reaction. As a consequence, obtained radical can react with O_2 or O_2•− and transform into hydroperoxide. Dehydration as a subsequent step leads to formation of 4,5-dioxopent-2-enoic acid. Li et al. emphasized that there is more than one acceptable ways for production of 4,5-dioxopent-2-enoic acid [73]. Furan derivatives obtained through rearrangement is next hydrolyzed to form 4-hydroxy-5-oxopent-2-enoic acid which can be oxidized to maleic acid. In present study it is suspected that hydroquinone degradation led to creation of maleic acid, which contains isotopically labeled carbon. Fumaric acid was also detected as derivatization compound from E/Z isomerization of maleic acid. Oh et al. described the possible mechanisms for *cis-trans* isomerization [77]. The most favored
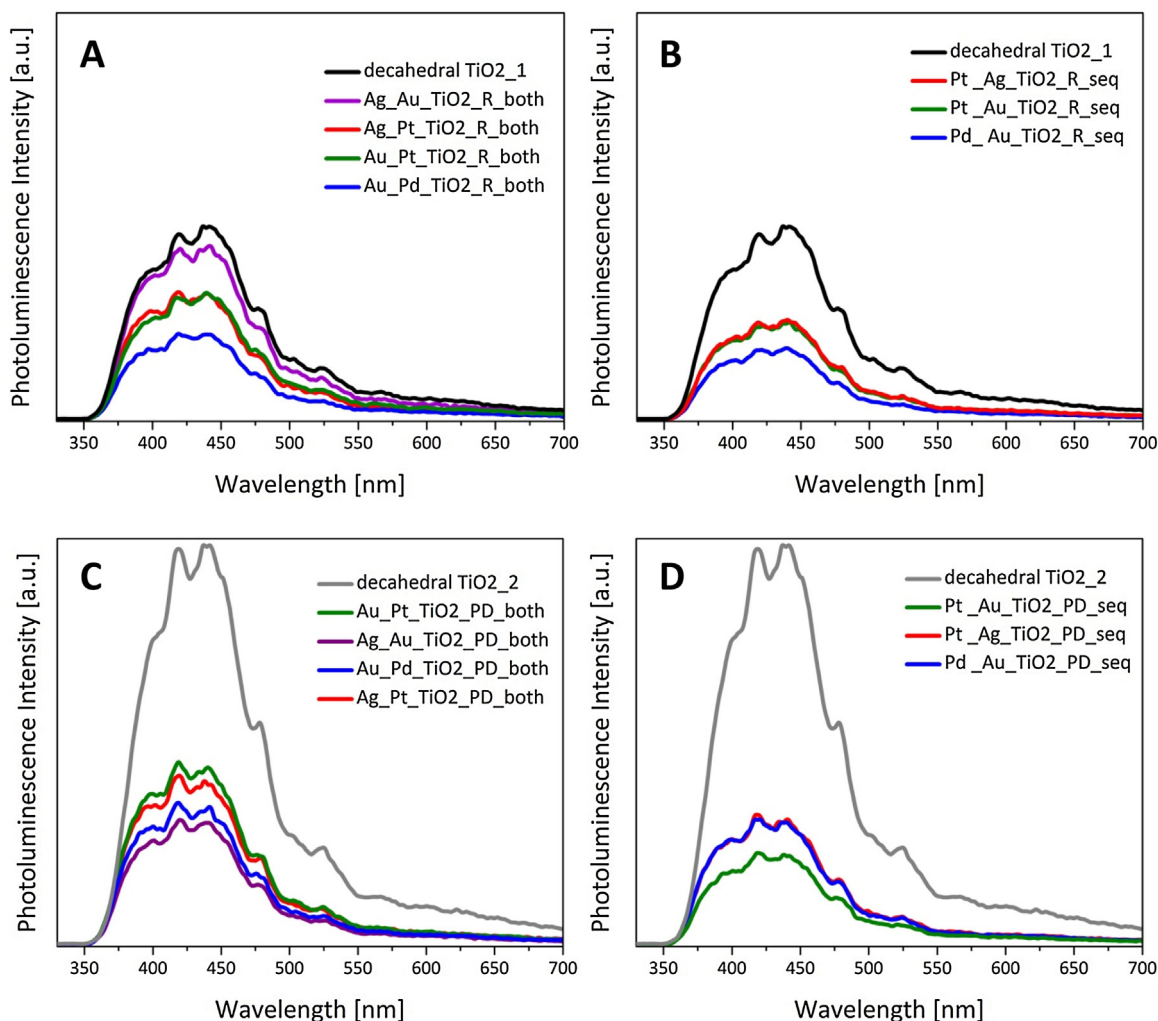
Fig. 5. Photoluminescence spectra of decahedral TiO₂ modified with bimetallic NPs obtained by (A) both and (B) seq radiolysis method and (C) both and (D) seq photodeposition method.

relies on creation of maleic acid radical anion, which is created by electron transfer from photoactivated TiO₂ to maleic acid [77]. They noticed that oxygenation caused isomerization efficiency loss, probably because oxygen acts as competitor electron acceptor. Oh et al. investigated further oxidation reaction of maleic and fumaric acid. They observed that tartaric, dihydroxyfumaric acid and other smaller intermediates were formed by hydroxyl attack [77]. Maleic acid can be reduced to succinic acid followed by oxidation to malonic and acetic acid. This observation is in good agreement with the present research carried out in the presence of Pt_Ag_TiO₂_PD_seq sample. Malonic acid formation was noticed during 300 min irradiation with applied light intensity equaled 24.3 mW/cm². The generated malonic acid was confirmed by the presence of *m/z* peak at 115 (relative abundance RA: 100, retention time Rt: 6.7 min).

Literature data show that pH has significant influence on the degradation mechanism of phenol. The effect of pH on the initial degradation rate of phenol in the presence of TiO₂ was studied [78]. Oliviera and Wei et al. suggested that the acceleration of degradation rate at high pH has been attributed to increased concentration of hydroxide and competitive adsorption [79,80]. In the opinion of Shea et al. at pH higher or equals 12 the oxide radical anion is responsible for oxidation pathway [78]. Additionally, Borji et al. investigated the effect of pH on the efficiency of phenol degradation [81]. They achieved the best results for suspension with initial pH 3 and inferior for pH 7. This is associated with higher concentration of hydrogen ions produced at lower pH, which can trigger formation of •OH radical. Guo et al. also reported that hydrogen ions have a significant influence on formation of •OH [82]. They complained that at pH above 11, phenol can be degraded by generation of phenolate anions. These species possess higher activity than phenol molecules.

Catechol molecule degradation proceeds analogously as in the case of hydroquinone by hydroxyl radicals attack, and reaction with O₂. This resulted in the production of o-semiquinone radicals which are oxidized later to *cis-cis*-muconic acid (hexa-2,4-dienedioic acid). Pillar et al. proved that it is possible to form 1,2,3- and 1,2,4-trihydroxybenzene[83]. It is predicted that formation of cis,cis-muconic acid should be preferred at lower pH, because at higher pH generation of trihydroxybenzene is privileged. Further degradation generates dioxoetane which decomposes into maleinaldehydic and glyoxylic acid. Maleinaldehydic acid is susceptible to hydroxyl radical attack and oxidation to maleic acid. As previously mentioned here also occurs transformation to fumaric acid. Oxidation of glyoxylic acid caused creation of oxalic acid. Decarboxylation product of oxalic acid resulted in formation of formic acid. Degradation of maleic acid proceeds analogously as in the previously described pathway I for hydroquinone oxidation. In the present study, we have identified also some traces

of 2-hydroxybenzoic acid. Although formation mechanism of 2-hydroxybenzoic acid is still not clear, its presence was reported in the few articles. Devlin at al also detected 2-hydroxybenzoic acid in there action mixture after degradation of phenol solution [84]. Also Sanchez et al. noticed presence of 2-hydroxybenzoic acid as well as resorcinol. Górska et al. identified hydroxybenzoic acid and aldehyde in the N,C/TiO_2 system under visible light irradiation [85]. Sclafani et al. examined synthesis of 2-hydroxybenzoic acid from CO_2 and phenol in the presence of pristine TiO_2 anatase or TiO_2 decorated with Pt or Cu [86]. They confirmed that salicylic acid can be formed by direct reaction with $^\bullet CO_2$ H radical. Our results showed appearance of some negligible amount of salicylic acid, but just like in case of Górska et al., we can't surely explain the formation mechanism of salicylic acid.

Aguilar et al. studied the degradation pathway of phenol in the presence of pristine TiO_2 and TiO_2-Fe_3O_4-M (M = Ag or Au) [87]. The pH of the solution (containing solvent mixture 50:50 methanol/water) was adjusted to 7.9. They observed that maximum reaction rate occurred at pH range between 3 and 5 and decreased at higher or lower pH values. At pH below 3 the generation of $^\bullet OH$ radicals was inhibited, because the positive holes in the valence band repulse the positive charged H_3O^+. At pH above 7 the surface of the photocatalysts absorbs OH^- ions, which hinder the absorption of phenol. The phenol oxidation products were analyzed by GC–MS after 8 h of irradiation. The results showed that benzoquinone is the major byproduct [87].

Dang et al. investigated the photodegradation pathways of phenol by commercial P25-TiO_2 [88]. The experiment was conducted using 100 ppm of phenol and $0.9 \, g/dm^3$ of TiO_2, the suspension was irradiated under UV-C light. Evaluation of produced byproducts was carried out by LC–MS, UV–vis spectrophotometer and photoluminescence technique. The results showed that absorbance peak of phenol decreased gradually during 16 h and afterwards decreased rapidly and vanished at 24 h of illumination [88]. They implied that this long time required for total degradation of phenol is attributed to high stability of benzene ring. Catechol and benzoquinone were formed after 3 h of illumination and had very high Pl intensity. Dang et al. detected more complex compounds as reaction products of two phenoxide ions, for instance 2-phenoxylcyclohexa-2,5-dienone, (1,10-biphenyl)-4-ol or tectoquinone [88]. These compounds were transformed readily back to catechol and benzoquinone. They reported that potentially $^\bullet OH$ radicals can attack benzene ring by addition of another OH group at the ortho and para position leads to formation of hydroxylhydroquinone and hydroxyl-benzoquinone. After the ring cleavage they observed formation of short chain hydrocarbon such as: glycerol, formic acid, oxalic acid, butanol, ethylene glycol and acetyl acid [88].

Zielinska et al. investigated phenol degradation by-product over Ag/Au-TiO_2 nanoparticles under Vis and UV–vis irradiation [34]. HPLC results showed that benzoquinone was the main intermediate product detected after 30 min of visible light irradiation. It was observed that the concentration of generated intermediate products: benzoquinone, hydroquinone, muconic acid, muconic aldehyde and oxalic acid increased during the first 3 h and then slowly decreased which indicated their further decomposition to the simple organic compounds. They observed that phenol, benzoquinone and hydroquinone almost disappeared after 5 h of irradiation over Ag/Au_TiO_2_5 nanoparticles [34].

Based on obtained results we can conclude in our findings that phenol degradation proceeds by hydroxyl radical. Oxidation of initial main byproducts (hydroquinone and catechol) results in formation of mixture of labeled and unlabeled maleic acid. This implied that the ring cleavage underwent between two different bonds and thus it is suggested that is more than one possible degradation pathway of hydroquinone and catechol. The presented data hasn't shown significant difference between type of sample and detected by-products.

3.6. Formation of hydroxyl radicals

The hydroxyl radical is one of the most chemically reactive species known and can be found in various media, so the photocatalytic activity of the samples studied was further confirmed by detection of $^\bullet OH$. Generation of $^\bullet OH$ at the BNPsTiO$_2$/water interface *via* photocatalytic reactions was assayed by reaction of the free radicals with coumarin to produce luminescent 7-hydroxycoumarin (7OHC), which has a fluorescence emission at 456 nm. Although the major hydroxylation product is 5-hydroxycoumarin, only 7-hydroxyproduct of coumarin hydroxylation emits fluorescent light [85,89,90].

Fig. 4 shows the changes in the PL intensity of coumarin under UV–vis irradiation with increasing irradiation time. The linear relationship between fluorescence intensity and irradiation time confirm the stability of obtained samples. In case of samples obtained by radiolysis method only the Pd_Au_TiO$_2$_R_seq sample showed two times higher rate of formation of $^\bullet OH$ radicals that pristine decahedral TiO_2, indicating that only for this sample BNPs surface modification enhances the production of free radicals (Fig. 4B).

Among of photocatalysts synthesized by photodeposition method when noble metals were added simultaneously (both) only Ag_Pt_TiO$_2$_PD_both and Ag_Au_TiO$_2$_PD_both showed higher rate of $^\bullet OH$ formation. At the same time, it is worth to noticed that all samples prepared by sequentially (seq) photodeposition method exhibit higher PL intensities compared to bare TiO_2 which suggests higher ability to form $^\bullet OH$ radicals (Fig. 4D). Based on this results it can be noticed that surface modification of TiO_2 with bimetallic nanoparticles by sequentially photodeposition method leads to an increase in the production of $^\bullet OH$ radicals under UV–vis light irradiation.

Fang et al. investigated the anatase TiO_2 single-crystal nanosheets (SCNSs) having 64% {001} facets were able to form $^\bullet OH$ on the surface of UV-illuminated TiO_2 with terephthalic acid used as a probe molecule [91]. They observed that synthesized TiO_2 SCNSs samples generated $^\bullet OH$ radicals five times larger than Degussa P25 TiO_2. Moreover, Liu at al demonstrated visible light photoactivity of N-doped anatase TiO_2 sheets with dominant {001} facets [92]. In contrast to undoped anatase TiO_2 sheets, the synthesized N-doped anatase TiO_2 sheets can generate $^\bullet OH$ radicals under 420−770 nm radiation, while only negligible $^\bullet OH$ radicals can be formed for undoped ones. However, Pan et al. noticed that anatase TiO_2 with predominant {001} facets compared with {010} and {101} facets, shows a lower reactivity which is inconsistent with previous reports [16]. Based on this results it can be concluded that more reliable theoretical and experimental evidence is needed to clarify the origin of this phenomenon. Moreover, Fang et al. noticed that other factors such as surface atomic/electronic structures, microfacets, dangling bonds, as well the typical crystal defects might be also critical to the photocatalytic performance [91].

3.7. PL emission spectra and the recombination of electron–hole

Photoluminescence (PL) emission was measured to understand the migration, transfer, and the recombination process of photogenerated electrons and holes [93]. With electron–hole pair recombination after a photocatalyst is irradiated, photons are emitted, resulting in photoluminescence signal [94,95]. Fig. 5 shows the PL spectra of all photocatalysts at 310 nm excitation light wavelength and in the wavelength range of 300–700 nm. Excitation peak at about 398 nm (3.12 eV) is attributed to the emission of band gap

of TiO$_2$ and coincided well with the absorption band edge in the diffuse reflection spectra in Fig. S2. The peak at 420 nm arising from the indirect band edge allowed transitions and self-trapped excitons localized in TiO$_6$ octahedra the peak at around 440 nm is due to charge transfer transition from Ti^{3+} to the O^{2-} in (TiO$_6$)$^{8-}$ [96,97]. Furthermore, the peaks at around 480 nm and 522 nm originate from oxygen vacancies and surface defects of TiO$_2$. These charge carriers are generally trapped by oxygen vacancies and surface hydroxyl groups, which contribute in their visible luminescence [98].

The lower PL intensity for the BNPs-TiO$_2$ samples indicates a relatively lower rate of electron and hole recombination which favors high photocatalytic activity. Modification of TiO$_2$ by metal nanoparticles leads to formation of Schottky barriers, which act as electron traps, facilitating electron–hole separation and promoting the interfacial electron transfer process, so recombination of photogenerated electron–hole pairs is more efficient after bimetallic modification. It can be observed that different efficiencies in electron scavenging, depending on the route of metal deposition can be noticed. Samples obtained by sequentially (seq) radiolysis and photodeposition method were more efficient in electron scavenging compared to the rest photocatalysts. The highest reduction in the charge carrier recombination was observed with modification with Pd and Au NPs – sample Pd_Au_TiO$_2$_R_seq. However, the same photocatalyst, prepared with the use of simultaneously synthesis (Pd_Au_TiO$_2$_R_both), showed higher recombination of photogenerated electron–hole pairs.

4. Conclusions

The decahedral TiO$_2$ nanoparticles prepared by hydrothermal method were decorated by noble metal nanoparticles. The influence of metal deposition method (simultaneous and subsequent) on metal nanocluster morphology and structure and its impact on TiO$_2$ photocatalytic activity under UV–vis irradiation was investigated for the first time. Moreover, our objective was to determine how the photocatalytic degradation pathways of phenol-1-^{13}C in the presence of BNPs-TiO$_2$ differ from that corresponding in the presence of pristine decahedral TiO$_2$. These comparisons were expected to provide some insight into the basic mechanism of the BNPs decorated TiO$_2$ and UV–vis light assisted water treatment. It can be concluded that:

- method of metal deposition (γ radiation *versus* UV photodeposition as well as subsequent (seq) or simultaneous (both) metal precursors introducing into reaction medium) has a significant influence on the photocatalytic activity
- all samples obtained by radiolytic reduction of BNPs showed superior photocatalytic properties compared to unmodified TiO$_2$. The highest photoactivity under UV–vis light irradiation was observed for Au_Pd_TiO$_2$_R_both and Pt_Ag_TiO$_2$_R_seq samples obtained by simultaneous and successive radiolytic reduction, respectively. The efficiency of phenol degradation after 90 min of irradiation was 73 and 76 %, respectively
- most samples obtained by photodeposition of BNPs showed the deterioration of photocatalytic activity in comparison to unmodified TiO$_2$, which could be attributed to the presence of O-vacancies created during calcination process of pristine decahedral TiO$_2$. Only sample Pt_Ag_TiO$_2$_PD_seq showed higher photoactivity (78% after 90 min of irradiation)
- photocatalytic process of isotopically labeled (1-^{13}C) phenol can be carried out by three different pathways
- phenol derivatives like catechol and benoquinone were consisted of only 1-^{13}C carbon isotope

- based on our results we can conclude that phenol degradation proceeds mainly by hydroxyl radical

Appendix A. Supplementary data

Supplementary data associated with this article can be found, in the online version, at http://dx.doi.org/10.1016/j.apcatb.2016.06.067.

References

[1] A. Fujishima, X. Zhang, D.A. Tryk, TiO$_2$ photocatalysis and related surface phenomena, Surf. Sci. Rep. 63 (2008) 515–582.
[2] K. Nakata, A. Fujishima, TiO$_2$ photocatalysis: design and applications, J. Photochem. Photobiol. C: Photochem. Rev. 13 (2012) 169–189.
[3] K. Hashimoto, H. Irie, A. Fujishima, TiO$_2$ photocatalysis: a historical overview and future prospects, Jpn. J. Appl. Phys. Part 1 Regul. Pap. Short Notes Rev. Pap. 44 (2005) 8269.
[4] H. Peng, X. Wang, G. Li, H. Pang, X. Chen, Facile synthesis of rice-like anatase TiO2 nanocrystals, Mater. Lett. 64 (2010) 1898–1901.
[5] N. Liu, Y. Zhao, X. Wang, H. Peng, G. Li, Facile synthesis and enhanced photocatalytic properties of truncated bipyramid-shaped anatase TiO$_2$ nanocrystals, Mater. Lett. 102 (2013) 53–55.
[6] R. Wang, X. Cai, F. Shen, Preparation of TiO$_2$ hollow microspheres by a novel vesicle template method and their enhanced photocatalytic properties, Ceram. Int. 39 (2013) 9465–9470.
[7] X. Wang, H. He, Y. Chen, J. Zhao, X. Zhang, Appl. Surf. Sci. 258 (2012) 5863–5868.
[8] M. Liu, H. Li, Y. Zeng, T. Huang, Anatase TiO$_2$ single crystals with dominant {001} facets: facile fabrication from Ti powders and enhanced photocatalytical activity, Appl. Surf. Sci. 274 (2013) 117–123.
[9] L. Jiang, Y. Zhong, G. Li, A simple H2O2-assisted route to hollow TiO2 structures with different crystal structures and morphologies, Mater. Res. Bull. 44 (2009) 999–1002.
[10] Y. Dai, C.M. Cobley, J. Zeng, Y. Sun, Y. Xia, Synthesis of anatase TiO2 nanocrystals with exposed {001} facets, Nano Lett. 9 (2009) 2455–2459.
[11] X. Han, Q. Kuang, M. Jin, Z. Xie, L. Zheng, Synthesis of titania nanosheets with a high percentage of exposed (001) facets and related photocatalytic properties, J. Am. Chem. Soc. 131 (2009) 3152–3153.
[12] L. Wang, L. Zang, J. Zhao, C. Wang, Green synthesis of shape-defined anatase TiO2 nanocrystals wholly exposed with {001} and {100} facets, Chem. Commun. 48 (2012) 11736–11738.
[13] V.M. Menéndez-Flores, M. Nakamura, T. Kida, Z. Jin, N. Murakami, T. Ohno, Controlled structure of anatase TiO2 nanoparticles by using organic additives in a microwave process, Appl. Catal. A: Gen. 406 (2011) 119–123.
[14] U. Diebold, The surface science of titanium dioxide, Surf. Sci. Rep. 48 (2003) 53–229.
[15] H.G. Yang, C.H. Sun, S.Z. Qiao, J. Zou, G. Liu, S.C. Smith, H.M. Cheng, G.Q. Lu, Anatase TiO2 single crystals with a large percentage of reactive facets, Nature 453 (2008) 638–641.
[16] J. Pan, G. Liu, G.Q.M. Lu, H.M. Cheng, On the true photoreactivity order of {001}, {010}, and {101} facets of anatase TiO2 crystals, Angew. Chem. Int. Ed. 50 (2011) 2133–2137.
[17] T. Tachikawa, S. Yamashita, T. Majima, Evidence for crystal-face-dependent TiO2 photocatalysis from single-molecule imaging and kinetic analysis, J. Am. Chem. Soc. 133 (2011) 7197–7204.
[18] N. Murakami, Y. Kurihara, T. Tsubota, T. Ohno, Shape-controlled anatase titanium(IV) oxide particles prepared by hydrothermal treatment of peroxo titanic acid in the presence of polyvinyl alcohol, J. Phys. Chem. C 113 (2009) 3062–3069.
[19] G. Liu, C.Y. Jimmy, G.Q.M. Lu, H.-M. Cheng, Crystal facet engineering of semiconductor photocatalysts: motivations, advances and unique properties, Chem. Commun. 47 (2011) 6763–6783.
[20] X.-Q. Gong, A. Selloni, Reactivity of anatase TiO2 nanoparticles: the role of the minority (001) surface, J. Phys. Chem. B 109 (2005) 19560–19562.
[21] Q. Wu, M. Liu, Z. Wu, Y. Li, L. Piao, Is photooxidation activity of {001} facets truly lower than that of {101} facets for anatase TiO2 crystals? J. Phys. Chem. C 116 (2012) 26800–26804.
[22] E. Grabowska, M. Diak, M. Marchelek, A. Zaleska, Decahedral TiO2 with exposed facets: synthesis, properties, photoactivity and applications, Appl. Catal. B: Environ. 156 (2014) 213–235.

[23] H.G. Yang, G. Liu, S.Z. Qiao, C.H. Sun, Y.G. Jin, S.C. Smith, J. Zou, H.M. Cheng, G.Q. Lu, Solvothermal synthesis and photoreactivity of anatase TiO2 nanosheets with dominant {001} facets, J. Am. Chem. Soc. 131 (2009) 4078–4083.

[24] D. Zhang, G. Li, H. Wang, K.M. Chan, J.C. Yu, Biocompatible anatase single-crystal photocatalysts with tunable percentage of reactive facets, Cryst. Growth Des. 10 (2010) 1130–1137.

[25] A. Zaleska-Medynska, M. Marchelek, M. Diak, E. Grabowska, Noble metal-based bimetallic nanoparticles: the effect of the structure on the optical, catalytic and photocatalytic properties, Adv. Colloid Interface Sci. 229 (2015) 80–107.

[26] A. Zielińska-Jurek, Progress, challenge, and perspective of bimetallic TiO2-based photocatalysts, J. Nanomater. 2014 (2014).

[27] Z. Hai, N.E. Kolli, J. Chen, H. Remita, Radiolytic synthesis of Au–Cu bimetallic nanoparticles supported on TiO2: application in photocatalysis, N. J. Chem. 38 (2014) 5279–5286.

[28] N. Toshima, T. Yonezawa, Bimetallic nanoparticles—novel materials for chemical and physical applications, N. J. Chem. 22 (1998) 1179–1201.

[29] A. Gołąbiewska, W. Lisowski, M. Jarek, G. Nowaczyk, A. Zielińska-Jurek, A. Zaleska, Visible light photoactivity of TiO2 loaded with monometallic (Au or Pt) and bimetallic (Au/Pt) nanoparticles, Appl. Surf. Sci. 317 (2014) 1131–1142.

[30] A. Cybula, G. Nowaczyk, M. Jarek, A. Zaleska, Preparation and characterization of Au/Pd modified-TiO2 photocatalysts for phenol and toluene degradation under visible light—the effect of calcination temperature, J. Nanomater. 2014 (2014).

[31] A. Cybula, J.B. Priebe, M.-M. Pohl, J.W. Sobczak, M. Schneider, A. Zielińska-Jurek, A. Brückner, A. Zaleska, The effect of calcination temperature on structure and photocatalytic properties of Au/Pd nanoparticles supported on TiO2, Appl. Catal. B: Environ. 152 (2014) 202–211.

[32] Y. Mizukoshi, K. Sato, T.J. Konno, N. Masahashi, Dependence of photocatalytic activities upon the structures of Au/Pd bimetallic nanoparticles immobilized on TiO2 surface, Appl. Catal. B: Environ. 94 (2010) 248–253.

[33] A. Zaleska-Medynska, M. Marchelek, M. Diak, E. Grabowska, Noble metal-based bimetallic nanoparticles: the effect of the structure on the optical, catalytic and photocatalytic properties, Adv. Colloid Interface Sci. 229 (2016) 80–107.

[34] A. Zielińska-Jurek, E. Kowalska, J.W. Sobczak, W. Lisowski, B. Ohtani, A. Zaleska, Preparation and characterization of monometallic (Au) and bimetallic (Ag/Au) modified-titania photocatalysts activated by visible light, Appl. Catal. B: Environ. 101 (2011) 504–514.

[35] A. Zielińska-Jurek, J. Hupka, Preparation and characterization of Pt/Pd-modified titanium dioxide nanoparticles for visible light irradiation, Catal. Today 230 (2014) 181–187.

[36] E. Kowalska, M. Janczarek, L. Rosa, S. Juodkazis, B. Ohtani, Mono-and bi-metallic plasmonic photocatalysts for degradation of organic compounds under UV and visible light irradiation, Catal. Today 230 (2014) 131–137.

[37] R. Su, R. Tiruvalam, Q. He, N. Dimitratos, L. Kesavan, C. Hammond, J.A. Lopez-Sanchez, R. Bechstein, C.J. Kiely, G.J. Hutchings, Promotion of phenol photodecomposition over TiO2 using Au, Pd, and Au–Pd nanoparticles, ACS Nano 6 (2012) 6284–6292.

[38] Y. Luo, S. Yu, B. Li, L. Dong, F. Wang, M. Fan, F. Zhang, Synthesis of (Ag, F)-modified anatase TiO2 nanosheets and their enhanced photocatalytic activity, N. J. Chem. 40 (2016) 2135–2144.

[39] L. Nie, P. Zhou, J. Yu, M. Jaroniec, Deactivation and regeneration of Pt/TiO2 nanosheet-type catalysts with exposed (001) facets for room temperature oxidation of formaldehyde, J. Mol. Catal. A: Chem. 390 (2014) 7–13.

[40] W. Chen, Q. Kuang, Q. Wang, Z. Xie, Engineering a high energy surface of anatase TiO2 crystals towards enhanced performance for energy conversion and environmental applications, RSC Adv. 5 (2015) 20396–20409.

[41] A. Sadovnikov, A. Baranchikov, Y. Zubavichus, O. Ivanova, V. Murzin, V.V. Kozik, V. Ivanov, Photocatalytically active fluorinated nano-titania synthesized by microwave-assisted hydrothermal treatment, J. Photochem. Photobiol. A: Chem. 303 (2015) 36–43.

[42] J. Rodríguez-Carvajal, Recent advances in magnetic structure determination by neutron powder diffraction, Physica B 192 (1993) 55–69.

[43] M. Diak, E. Grabowska, A. Zaleska, Synthesis, characterization and photocatalytic activity of noble metal-modified TiO2 nanosheets with exposed {001} facets, Appl. Surf. Sci. 347 (2015) 275–285.

[44] G. Liu, H. Sun, H.G. Yang, S.C. Smith, L. Wang, G.Q. Lu, H.M. Cheng, Chem. Commun. 46 (2010) 755–757.

[45] Z. Wang, K. Lv, G. Wang, K. Deng, D. Tang, Study on the shape control and photocatalytic activity of high-energy anatase titania, Appl. Catal. B: Environ. 100 (2010) 378–385.

[46] M. D'Arienzo, J. Carbajo, A. Bahamonde, M. Crippa, S. Polizzi, R. Scotti, L. Wahba, F. Morazzoni, Photogenerated defects in shape-controlled TiO2 anatase nanocrystals: a probe to evaluate the role of crystal facets in photocatalytic processes, J. Am. Chem. Soc. 133 (2011) 17652–17661.

[47] J.-M. Wu, M.-L. Tang, Hydrothermal growth of nanometer-to micrometer-size anatase single crystals with exposed (001) facets and their ability to assist photodegradation of rhodamine B in water, J. Hazard. Mater. 190 (2011) 566–573.

[48] S. Zhu, S. Liang, Q. Gu, L. Xie, J. Wang, Z. Ding, P. Liu, Effect of Au supported TiO2 with dominant exposed {001} facets on the visible-light photocatalytic activity, Appl. Catal. B: Environ. 119 (2012) 146–155.

[49] T. Pakizeh, C. Langhammer, I. Zoric, P. Apell, M. Käll, Intrinsic Fano interference of localized plasmons in Pd nanoparticles, Nano Lett. 9 (2009) 882–886.

[50] A. Zielińska, E. Skwarek, A. Zaleska, M. Gazda, J. Hupka, Preparation of silver nanoparticles with controlled particle size, Procedia Chem. 1 (2009) 1560–1566.

[51] S. Tanuma, C. Powell, D. Penn, Calculations of electron inelastic mean free paths. IX. Data for 41 elemental solids over the 50 eV to 30 keV range, Surf. Interface Anal. 43 (2011) 689–713.

[52] P. Górska, A. Zaleska, E. Kowalska, T. Klimczuk, J.W. Sobczak, E. Skwarek, W. Janusz, J. Hupka, TiO2 photoactivity in Vis and UV light: the influence of calcination temperature and surface properties, Appl. Catal. B: Environ. 84 (2008) 440–447.

[53] H. Jensen, A. Soloviev, Z. Li, E.G. Sogaard, XPS and FTIR investigation of the surface properties of different prepared titania ano-powders, Appl. Surf. Sci. 246 (2005) 239–249.

[54] J. Yu, X. Zhao, Q. Zhao, Effect of surface structure on photocatalytic activity of TiO2 thin films prepared by sol–gel method, Thin Solid Films 379 (2000) 7–14.

[55] A. Naumkin, A. Kraut-Vass, S. Gaarenstroom, C. Powell, NIST X-ray Photoelectron Spectroscopy Database 20, Version 4.1, National Institute of Standards and Technology, Gaithersburg, 2012://srdata.nist.gov/xps (2012).

[56] A. Rjeb, S. Letarte, L. Tajounte, M.C. El Idrissi, A. Adnot, D. Roy, Y. Claire, J. Kaloustian, Polypropylene natural aging studied by X-ray photoelectron spectroscopy, J. Electron Spectrosc. Relat. Phenom. 107 (2000) 221–230.

[57] C. Tyson, A. Bzowski, P. Kristof, M. Kuhn, R. Sammynaiken, T. Sham, Charge redistribution in Au-Ag alloys from a local perspective, Phys. Rev. B 45 (1992) 8924.

[58] H.-P. Steinrück, F. Pesty, L. Zhang, T.E. Madey, Ultrathin films of Pt on TiO2 (110): Growth and chemisorption-induced surfactant effects, Phys. Rev. B 51 (1995) 2427.

[59] J. Zeng, J. Yang, J.Y. Lee, W. Zhou, Preparation of carbon-supported core–shell Au–Pt nanoparticles for methanol oxidation reaction: the promotional effect of the Au core, J. Phys. Chem. B 110 (2006) 24606–24611.

[60] A.T.N. Dao, D.M. Mott, K. Higashimine, S. Maenosono, Enhanced electronic properties of Pt@ Ag heterostructured nanoparticles, Sensors 13 (2013) 7813–7826.

[61] K. Schierbaum, S. Fischer, M. Torquemada, J. De Segovia, E. Roman, J. Martin-Gago, The interaction of Pt with TiO2 (110) surfaces: a comparative XPS, UPS, ISS, and ESD study, Surf. Sci. 345 (1996) 261–273.

[62] B. Iurascu, I. Siminiceanu, D. Vione, M.A. Vicente, A. Gil, Phenol degradation in water through a heterogeneous photo-Fenton process catalyzed by Fe-treated laponite, Water Res. 43 (2009) 1313–1322.

[63] A. Santos, P. Yustos, A. Quintanilla, F. Garcia-Ochoa, J. Casas, J. Rodriguez, Evolution of toxicity upon wet catalytic oxidation of phenol, Environ. Sci. Technol. 38 (2004) 133–138.

[64] E. Grabowska, J.W. Sobczak, M. Gazda, A. Zaleska, Surface properties and visible light activity of W-TiO2 photocatalysts prepared by surface impregnation and sol–gel method, Appl. Catal. B: Environ. 117 (2012) 351–359.

[65] M. Klein, J. Nadolna, A. Gołąbiewska, P. Mazierski, T. Klimczuk, H. Remita, A. Zaleska-Medynska, The effect of metal cluster deposition route on structure and photocatalytic activity of mono-and bimetallic nanoparticles supported on TiO2 by radiolytic method, Appl. Surf. Sci. 378 (2016) 37–48.

[66] J.J. Plata, A.M. Márquez, J.F. Sanz, R.S. Avellaneda, F. Romero-Sarria, M.I. Domínguez, M.A. Centeno, J.A. Odriozola, Gold nanoparticles on yttrium modified titania: support properties and catalytic activity, Top. Catal. 54 (2011) 219–228.

[67] T. Nishimura, T. Akita, Y. Kido, Electronic charge transfer between Au nano-particles and TiO2-terminated SrTiO3 (001) substrate, Surf. Sci. 604 (2016) 548–554.

[68] J. Schneider, M. Matsuoka, M. Takeuchi, J. Zhang, Y. Horiuchi, M. Anpo, D.W. Bahnemann, Understanding TiO2 photocatalysis: mechanisms and materials, Chem. Rev. 114 (2014) 9919–9986.

[69] M. Klein, J. Nadolna, A. Gołąbiewska, P. Mazierski, T. Klimczuk, H. Remita, A. Zaleska-Medynska, The effect of metal cluster deposition route on structure and photocatalytic activity of mono-and bimetallic nanoparticles supported on TiO2 by radiolytic method, Appl. Surf. Sci. 378 (2016) 37–48.

[70] H. Tada, A. Takao, T. Akita, K. Tanaka, Surface properties and photocatalytic activity of Ptcore/Agshell nanoparticle-loaded TiO2, ChemPhysChem 7 (2006) 1687–1691.

[71] H. Yu, X. Wang, H. Sun, M. Huo, Photocatalytic degradation of Malathion in aqueous solution using an Au–Pd–TiO2 nanotube film, J. Hazard. Mater. 184 (2010) 753–758.

[72] A. Sclafani, J.-M. Herrmann, Influence of metallic silver and of platinum–silver bimetallic deposits on the photocatalytic activity of titania (anatase and rutile) in organic and aqueous media, J. Photochem. Photobiol. A: Chem. 113 (1998) 181–188.

[73] X. Li, J.W. Cubbage, T.A. Tetzlaff, W.S. Jenks, Photocatalytic degradation of 4-chlorophenol. 1. The hydroquinone pathway, J. Org. Chem. 64 (1999) 8509–8524.

[74] N. Raghavan, S. Steenken, Electrophilic reaction of the hydroxyl radical with phenol. Determination of the distribution of isomeric dihydroxycyclohexadienyl radicals, J. Am. Chem. Soc. 102 (1980) 3495–3499.

[75] E. Mvula, M.N. Schuchmann, C. von Sonntag, Reactions of phenol-OH-adduct radicals phenoxyl radical formation by water elimination vs. oxidation by dioxygen, J. Chem. Soc. Perkin Trans. 2 (2001) 264–268.

[76] C. Richard, Photocatalytic reduction of benzoquinone in aqueous ZnO or TiO2 suspensions, N. J. Chem. 18 (1994) 443–445.

[77] Y.-C. Oh, X. Li, J.W. Cubbage, W.S. Jenks, Mechanisms of catalyst action in the TiO2-mediated photocatalytic degradation and *cis–trans* isomerization of maleic and fumaric acid, Appl. Catal. B: Environ. 54 (2004) 105–114.

[78] K.E. O'Shea, C. Cardona, The reactivity of phenol in irradiated aqueous suspensions of TiO2. Mechanistic changes as a function of solution pH, J. Photochem. Photobiol. A: Chem. 91 (1995) 67–72.

[79] J.C. D'Oliveira, G. Al-Sayyed, P. Pichat, Photodegradation of 2-and 3-chlorophenol in titanium dioxide aqueous suspensions, Environ. Sci. Technol. 24 (1990) 990–996.

[80] T.-Y. Wei, C.-c. Wan, Kinetics of photocatalytic oxidation of phenol on TiO2 surface, J. Photochem. Photobiol. A: Chem. 69 (1992) 241–249.

[81] S.H. Borji, S. Nasseri, A.H. Mahvi, R. Nabizadeh, A.H. Javadi, Investigation of photocatalytic degradation of phenol by Fe(III)-doped TiO2 and TiO2 nanoparticles, J. Environ. Health Sci. Eng. 12 (2014) 1.

[82] Z. Guo, R. Ma, G. Li, Degradation of phenol by nanomaterial TiO2 in wastewater, Chem. Eng. J. 119 (2006) 55–59.

[83] E.A. Pillar, R.C. Camm, M.I. Guzman, Catechol oxidation by ozone and hydroxyl radicals at the air–water interface, Environ. Sci. Technol. 48 (2014) 14352–14360.

[84] H.R. Devlin, I.J. Harris, Mechanism of the oxidation of aqueous phenol with dissolved oxygen, Ind. Eng. Chem. Fundam. 23 (1984) 387–392.

[85] P. Górska, A. Zaleska, J. Hupka, Photodegradation of phenol by UV/TiO2 and Vis/N, C-TiO2 processes: comparative mechanistic and kinetic studies, Sep. Purif. Technol. 68 (2009) 90–96.

[86] A. Sclafani, L. Palmisano, G. Farneti, Synthesis of 2-hydroxybenzoic acid from CO2 and phenol in aqueous heterogeneous photocatalytic systems, Chem. Commun. (1997) 529–530.

[87] C.H. Aguilar, T. Pandiyan, J. Arenas-Alatorre, N. Singh, Oxidation of phenols by TiO2 Fe3O4 M (M = Ag or Au) hybrid composites under visible light, Sep. Purif. Technol. 149 (2015) 265–278.

[88] T.T.T. Dang, S. Le, D. Channei, W. Khanitchaidecha, A. Nakaruk, Photodegradation mechanisms of phenol in the photocatalytic process, Res. Chem. Intermed. (2016) 1–14.

[89] G. Louit, S. Foley, J. Cabillic, H. Coffigny, F. Taran, A. Valleix, J.P. Renault, S. Pin, The reaction of coumarin with the OH radical revisited: hydroxylation product analysis determined by fluorescence and chromatography, Radiat. Phys. Chem. 72 (2005) 119–124.

[90] H. Czili, A. Horváth, Applicability of coumarin for detecting and measuring hydroxyl radicals generated by photoexcitation of TiO2 nanoparticles, Appl. Catal. B: Environ. 81 (2008) 295–302.

[91] G. Liu, H.G. Yang, X. Wang, L. Cheng, J. Pan, G.Q. Lu, H.-M. Cheng, J. Phys. Chem. Lett. 2 (2011) 725–734.

[92] G. Liu, H.G. Yang, X. Wang, L. Cheng, J. Pan, G.Q. Lu, H.-M. Cheng, Visible light responsive nitrogen doped anatase TiO2 sheets with dominant {001} facets derived from TiN, J. Am. Chem. Soc. 131 (2009) 12868–12869.

[93] M.A. Henderson, A surface science perspective on photocatalysis, Surf. Sci. Rep. 66 (2011) 185–297.

[94] J. Liqiang, Q. Yichun, W. Baiqi, L. Shudan, J. Baojiang, Y. Libin, F. Wei, F. Honggang, S. Jiazhong, Review of photoluminescence performance of nano-sized semiconductor materials and its relationships with photocatalytic activity, Sol. Energy Mater. Sol. Cells 90 (2006) 1773–1787.

[95] L. Kernazhitsky, V. Shymanovska, T. Gavrilko, V. Naumov, L. Fedorenko, V. Kshnyakin, J. Baran, Room temperature photoluminescence of anatase and rutile TiO2 powders, J. Lumin. 146 (2014) 199–204.

[96] H. Tang, H. Berger, P.E. Schmid, F. Lévy, G. Burri, Photoluminescence in TiO2 anatase single crystals, Solid State Commun. 87 (1993) 847–850.

[97] J. Yu, H. Yu, C. Ao, S. Lee, C.Y. Jimmy, W. Ho, Preparation, characterization and photocatalytic activity of in situ Fe-doped TiO2 thin films, Thin Solid Films 496 (2006) 273–280.

[98] S. Mathew, A. kumar Prasad, T. Benoy, P. Rakesh, M. Hari, T. Libish, P. Radhakrishnan, V. Nampoori, C. Vallabhan, UV-visible photoluminescence of TiO2 nanoparticles prepared by hydrothermal method, J. Fluoresc. 22 (2012) 1563–1569.